Parametric Systems Analysis of a Mid-Lift/Drag Entry System for Human Mars Mission

Jamshid A. Samareh[*], Michael P. Behrend[†], Carl C. Poteet[‡], D. R. Komar[§], John E. Theisinger[**], Rafael A. Lugo[††]
NASA Langley Research Center, Hampton, Virginia 23681

Jeffery V. Bowels[‡‡]
NASA Ames Research Center, Moffett Field, CA, 94035

Mars entry systems are complex with many competing design objectives. This paper presents a data-driven and physics-based approach to systems analysis and tradespace exploration for a human Mars entry system using a Mid-Lift/Drag aerodynamic decelerator. The baseline entry system includes elements for Mars aerocapture, entry, descent, and landing segments of the mission. The approach uses a set of parametric models that enable a system-level analysis, vehicle sizing, sensitivity analysis, and tradespace exploration. The paper provides a brief introduction of the Mid-Lift/Drag concept, an overview of parametric models, discussions on alternative structural concepts, results from system-level analysis, and summary remarks.

I. Introduction

The plan for human missions to Mars has gone through many changes since the 1950s (Portree, 2001). Von Braun developed the first detailed mission study published in West Germany in 1952 (von Braun, 1952), followed by an English version in 1962. The von Braun mission concept required ten 4,000-ton ships with 70 crewmembers, requiring over five million tons of propellant, equivalent to propellant required for about 2000 Saturn Vs. The mission concept used wheeled gliders that would land horizontally. The study assumed an earlier atmospheric model, prior to the Mariner 4 spacecraft mission discovery that Mars atmosphere was thinner than expected by a factor of 10. It is impractical to use horizontal landers for human scale missions in such a thin atmosphere.

NASA has performed several in-depth studies of the human Mars missions. The design reference architecture 5.0 (Drake, 2009) is a large NASA study that provides the most recent common framework for future planning of systems, concepts, and technology development. Drake and Watts (2014) provide an update to the study performed in 2009. The NASA studies have identified the Entry, Descent, and Landing (EDL) system as one the most critical elements of the entire architecture. Subsequently, NASA commissioned a follow on EDL Systems Analysis (EDL-SA) study to identify a roadmap needed to successfully land large payloads on Mars for both robotic (Ivanov et al., 2011) and human-scale missions (Dwyer Cianciolo et al., 2010). One of the concepts used for the EDL-SA study employed a Mid-Lift/Drag (L/D) entry system. For the EDL-SA study, Samareh and Komar (2011) developed an approach for the EDL parametric modeling that is the basis for this paper.

---

[*] Aerospace Engineer, Vehicle Analysis Branch (E401), AIAA Associate Fellow.
[†] Aerospace Engineer, Structural & Thermal Systems Branch (D206).
[‡] Aerospace Engineer, Structural Mechanics & Concepts Branch (D312).
[§] Aerospace Engineer, Vehicle Analysis Branch (E401), AIAA Senior Member.
[**] Aerospace Engineer, Atmospheric Flight & Entry Systems Branch (D205), AIAA Senior Member.
[††] Aerospace Engineer, Atmospheric Flight & Entry Systems Branch (D205), AIAA Member.
[‡‡] Aerospace Engineer, Systems Analysis Office, AIAA Senior Member.

Polsgrove et al. (2016) provide a summary of the Evolvable Mars Campaign (EMC) with a focus on the effects of mission and vehicle design options on lander mass and performance. NASA has studied Mars entry systems for four different aerodynamic decelerator configurations: Hypersonic Inflatable Aerodynamic Decelerator (HIAD) (Polsgrove et al., 2017), Mid-L/D (Cerimele et al., 2017), Adaptive Deployable Entry and Placement Technology (ADEPT) (Cassell et al., 2017), and a traditional capsule concept (Price et al., 2016). Each entry system includes an aerodynamic decelerator, a Mars Descent Module (MDM), and a 20-t payload. Polsgrove et al. (2017) provide the basic study assumptions and constraints. Lillard et al. (2017) present an assessment of the major risks associated with developing a human scale architecture to sustain a human presence on Mars.

Cerimele et al. (2017) chronicle the evolution of the Mid-L/D entry system (Figure 1). The early Mid-L/D concepts used an ellipsled roughly the shape of a payload fairing of a launch vehicle. However, the current concept is similar to the Space Shuttle main body. Compared to the low L/D concepts (e.g., HIAD), the Mid-L/D concept has improved downrange and cross range capability with a wider entry corridor width and potentially better landing accuracy. Cerimele et al. (2017) discuss the Mid-L/D benefits such as reduction in design, development, test, and evaluation cost; leveraging proven tools, materials, control approaches, and design/verification processes.

This paper presents a data-driven and physics-based systems analysis and tradespace exploration for a human Mars entry system using Mid-L/D aerodynamic decelerators. The following sections summarize the systems analysis for the Mid-L/D entry system and provide details of the Mid-L/D concept, parametric systems analysis, and alternative structures concepts. The last two sections include a discussion of results and concluding remarks.

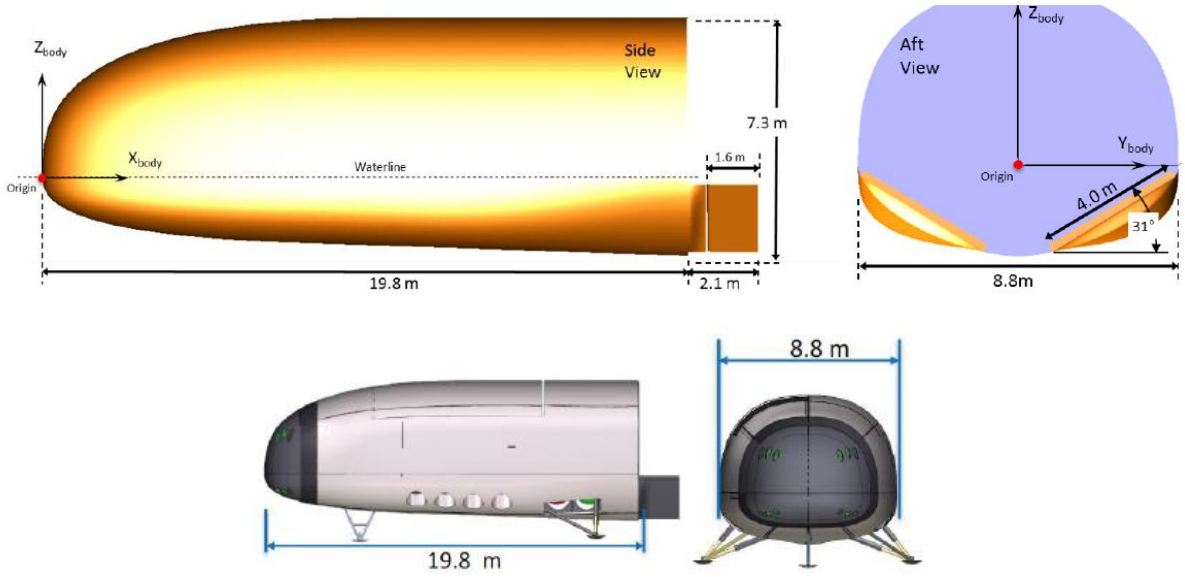

Figure 1 Mid-L/D vehicle outer mold line (OML).

II. The Mid-L/D Entry System Concept

Cerimele et al. (2017) provides an excellent overview of the Mid-L/D baseline concept. The CobraMRV-2908b version of the Mid-L/D is the focus of this study. Figure 2 shows cutaways with the Mars Ascent Vehicle (MAV) as the primary payload, the MDM consisting of primary and secondary structures, tanks, and engines. Unlike previous Mid-L/D studies (Dwyer Ciancolo et al. 2010), the current baseline concept of operations (ConOps) retains its aeroshell through the entire mission, eliminating the risk and complexity associated with the jettison process. In addition to a simpler descent, keeping the aeroshell provides an effective protection for the payload during the EDL phase of the mission. The rigid aeroshell also houses a set of Supersonic Retro Propulsion (SRP) engines.

Concept of Operations (ConOps)

Figure 3 shows the Mid-L/D configurations during all mission phases (Polsgrove et al., 2018). During launch, the Mid-L/D orientation is vertical inside the payload fairing. After reaching a high Earth orbit, the Mid-L/D docks with the in-space solar electric propulsion (SEP) transportation stage for transit to Mars. During transit, the vehicle receives power from the transportation system.

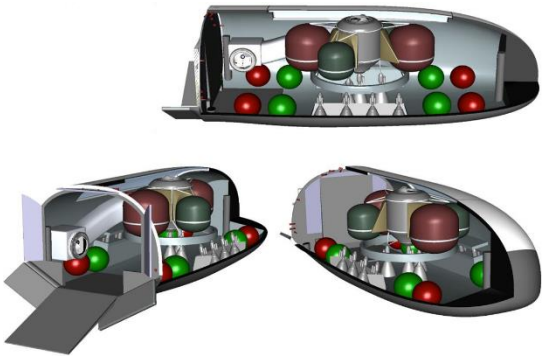

Figure 2 Cutaway views of the Mid-L/D vehicle.

Figure 4 shows nine phases of aerocapture and EDL. Two days before Mars arrival, the vehicle separates from the SEP and prepares for aerocapture into Mars orbit (phase 1). The vehicle arrives at Mars with a relative velocity of 6.2 km/s in a polar orbit (phase 2). The vehicle then performs an aerocapture into a Mars one solar (1-Sol) day orbit using its Reaction Control System (RCS) thrusters and body flaps (phase 3), followed by periapsis raise (phase 4) and apoapsis and plane change correction (phase 5). After aerocapture, the lander provides power during Mars orbit loiter for up to one year (phase 6). Before the EDL sequence initiation, the vehicle performs a final checkout followed by a deorbit burn using the RCS thrusters (phase 7). The hypersonic entry is a critical segment of the entire mission (phase 8), followed by the powered descent and landing segment (phase 9).

Figure 5 shows the EDL sequence with a deorbit burn at the apoapsis of the parking orbit (Polsgrove et al., 2018). The vehicle enters with an angle of attack near 55°. After hypersonic entry and at approximately Mach 2, the vehicle changes its attitude to angle of attack of 90° and initiates the SRP engines for descent and touchdown. The vehicle maintains a constant velocity of 2.5 m/s for 5 seconds prior to landing at 0 km altitude relative to the Mars Orbiter Laser Altimeter (MOLA) ellipsoid, within 50 m radius of the desired site. Once on the surface, radiators provide thermal management of the cryogenic storage facility on the MAV lander. The lander has batteries to support operations on the surface for 24 hours, allowing time to connect to a previously landed surface power supply.

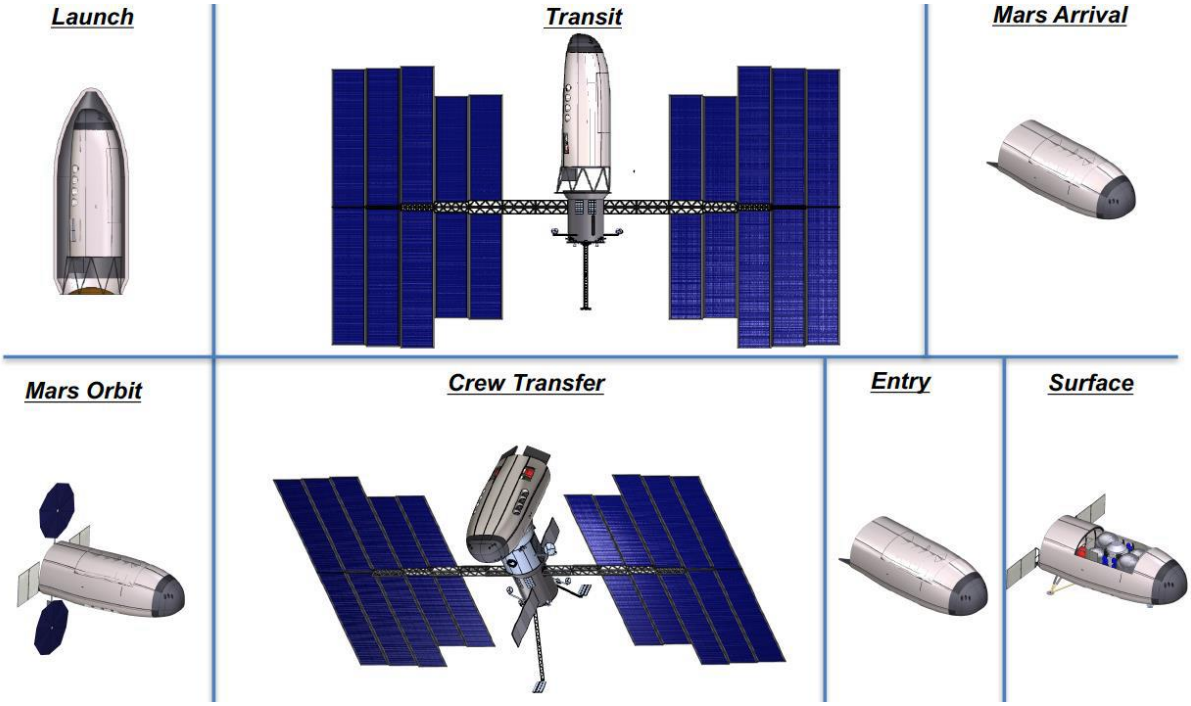

Figure 3 The Mid-L/D configurations during mission phases.

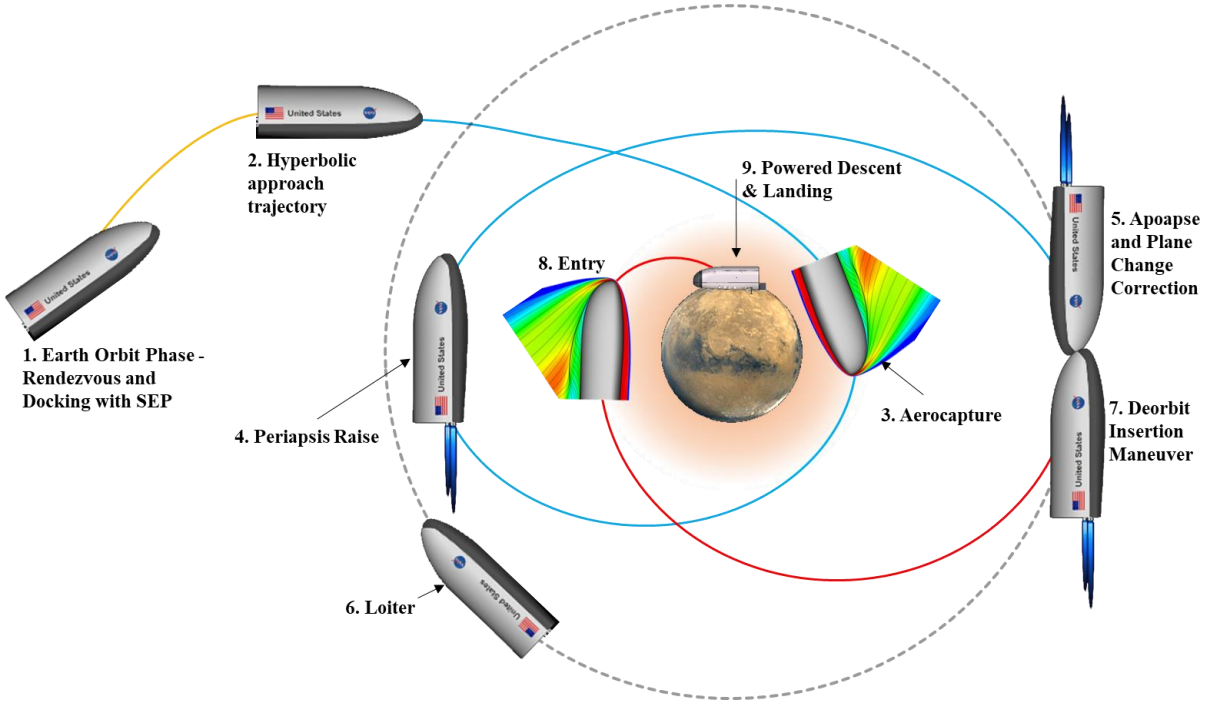

Figure 4 Aerocapture and EDL phases.

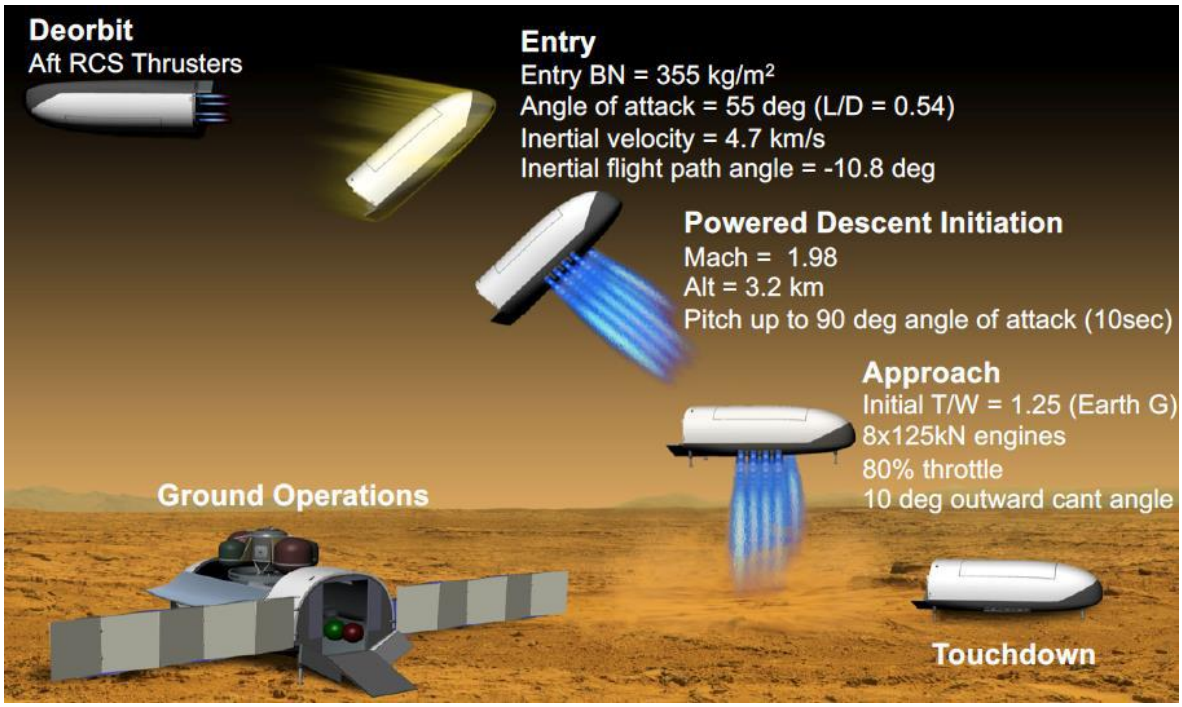

Figure 5 The Mid-L/D baseline EDL phases.

III. Parametric Systems Analysis

Parametric systems analysis (SA) and tradespace exploration provide a holistic view of systems and concepts, and they provide decision makers with a better understanding of various entry system concepts and their limitations based on quantitative data. The traditional SA process may take from several weeks to several years. Automating and streamlining the analysis method are the essential ingredients of the approach used in this paper. This approach has significantly improved the process and reduced the errors resulting from the manual data transfer among discipline experts. The improved process has accelerated the analysis and design activities such as tradespace studies, sensitivity analyses, Monte Carlo analyses, and vehicle optimization.

Parametric models are the building blocks of an efficient SA. A parametric model relates the vehicle component properties (e.g., mass) to vehicle dimensions and key mission parameters (e.g., entry velocity). The availability of parametric models is a key component for improving the SA process. The approach used in this study is a modified version of the work proposed by Samareh (2009) and Samareh and Komar (2011).

The solution procedures follow the notional phases shown in Figure 4. The initial solution iteration starts with a vehicle mass at Earth orbit rendezvous and docking with the SEP (phase 1). Phase 2 is the Trans-Mars Injection (TMI) with an assumption on RCS burns prior to aerocapture. Using arrival conditions, trajectory analyses for aerocapture and EDL segments provide the necessary environmental data such as heat flux profiles, maximum dynamic pressures, and g-loadings for entry and aerocapture. The data is then used to calculate the thermal protection system (TPS) and structures masses. Using the ΔV requirements from flight mechanics, Exploration Architecture Model for the IN-space and Earth-to-orbit modeling (EXAMINE) (Komar et al., 2008) is used to estimate the required masses for propellant, RCS, engines, and subsystems. The entry system mass, excluding the payload, is calculated. The payload mass is the estimated arrival mass minus the calculated system mass. If the difference between the estimated payload mass and target payload mass is not within a tolerance, the arrival mass is adjusted and the solution iteration is repeated until convergence is achieved. It usually takes four to five iterations to converge to a consistent mass breakdown and less than five minutes on a standard laptop computer. The following subsections provide descriptions of the parametric models used in this study.

A. Structures Model

A parametric scripting process is used to size the baseline finite-element model (FEM) of the CobraMRV-2908b (Calderon et al., 2020) to determine the structural mass sensitivity to changes in certain design and loading parameters. The FEM was created using commercial software[*] Pro Engineer[†] Computer Aided Drawing (CAD) and MacNeal-Schwendler Corporation (MSC) Patran software[‡]. MSC Nastran is used as the linear solver (SOL 101) and Collier Research Hypersizer[§] is used for structural sizing optimization. Python is used as the scripting language to tie the various programs together for a fully automated parametric sizing-optimization cycle. Figure 6 shows the baseline FEM.

Four load cases and nine mass constants were included in this study, along with vehicle scaling factors. The load cases and scaling/mass variables investigated in this study are shown in Figure 7, Table 1, and Table 2 with their assumed baseline values.

Load variables are incorporated by parsing and altering the Nastran input deck. For load case 2, the pressure field at maximum dynamic pressure is mapped on the Outer Mold Line (OML) by utilizing modified Newtonian theory for inviscid flow to generate local pressure coefficients for each element. Scaling alterations to the baseline FEM are accomplished with MSC Patran Command Language (PCL). Mass variables are changed by smearing the density of the respective FEM components to achieve the target mass. Sizing optimization is performed by utilizing Hypersizer's scripting Application Programming Interface (API). A prepopulated baseline Hypersizer database is used as a sizing template and serves as the sizing optimization input file to the Python script. Structural sizing in this study assumes aluminum 2219 construction. Table 3 lists other Hypersizer assumptions.

[*] Use of commercial software is not an endorsement by NASA.
[†] http://www.ptc.com/
[‡] https://www.mscsoftware.com/
[§] https://hypersizer.com/

The structural mass sensitivity to input parameters was determined after running approximately 500 cases through the Python script. Figure 8 shows the results of this sensitivity analysis. Note that certain variables such as angle of attack and sideslip angle have a negligible effect on structural mass and are not listed. The results are interpreted as the percent change in total structural mass due to a 1% change in the corresponding input parameters. For example, the mass variable with the highest sensitivity on the total structural mass was the mass of Mars Ascent Vehicle (MAV). A 1% increase in MAV mass corresponds to a 0.2% increase in the structural mass of the vehicle. Similarly, the sensitivity of individual structural property regions for each investigated variable are further broken out and shown in Table 4.

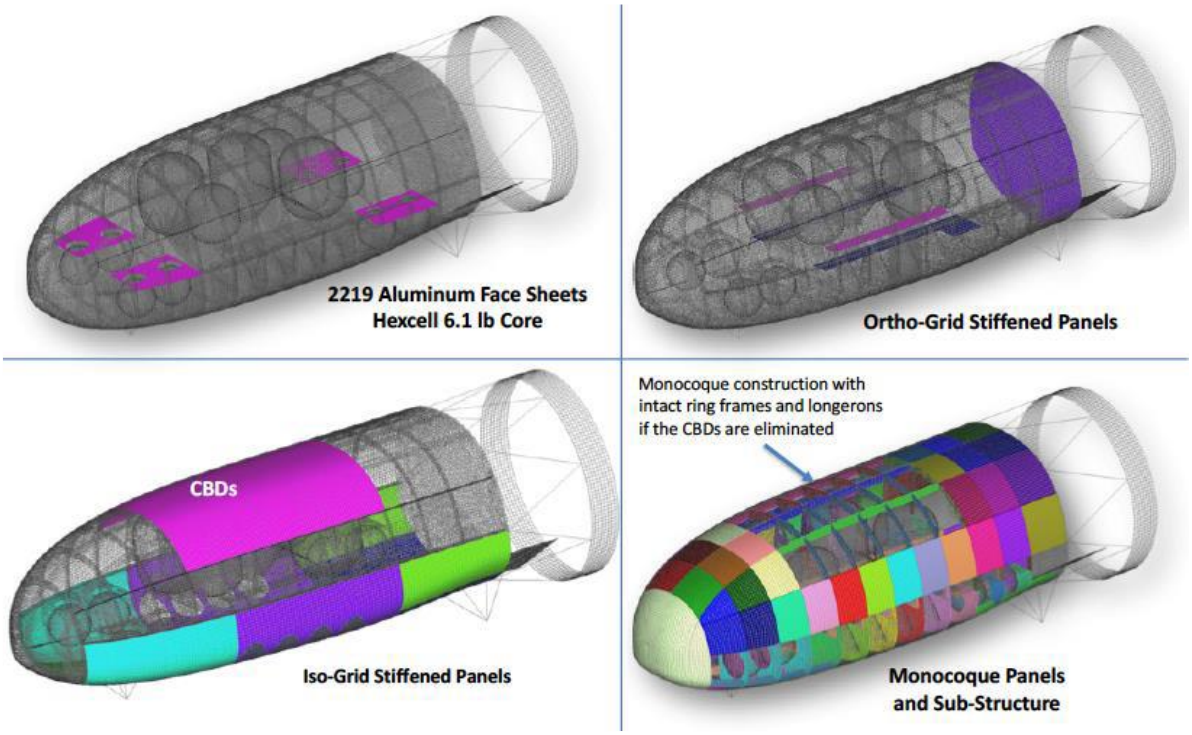

Figure 6 Structural concept for the Mid-L/D with cargo bay door (Polsgrove et al., 2018).

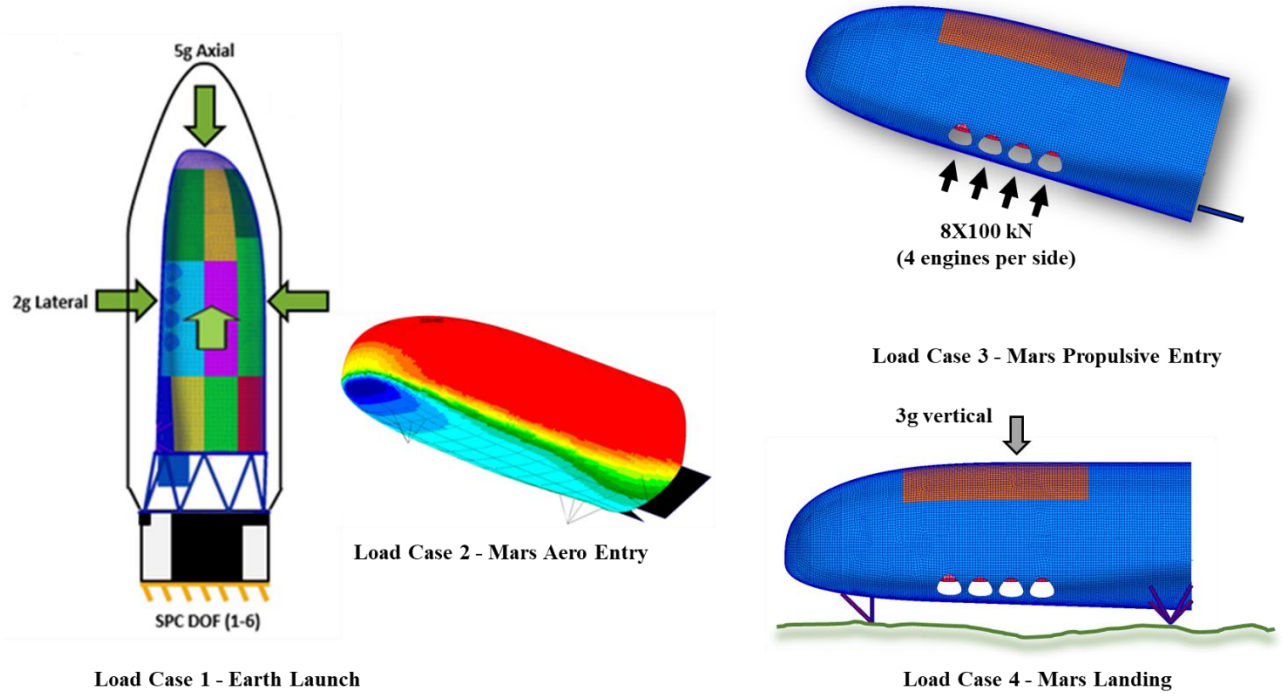

Figure 7 Load cases.

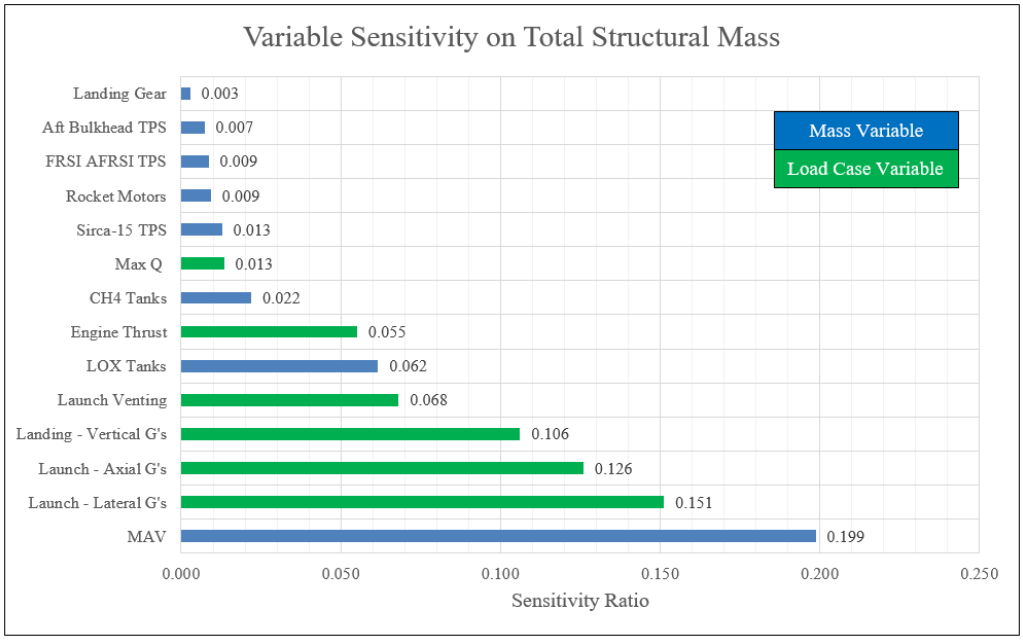

Figure 8 Variable sensitivity on total structural mass.

Table 1 Load case variables.

Variable	Baseline Value (English)	Baseline Value (SI)
Load Case 1 - Launch		
Axial G	5 g's	5 g's
Lateral G	2 g's	2 g's
Venting Pressure	0.5 psi	3450 Pa
Load Case 2 - Max Dynamic Pressure – Mars Entry		
Angle of Attack	55 deg	55 deg
Sideslip Angle	0 deg	0 deg
Mach #	20	20
Max Q	1 psi	6900 Pa
Load Case 3 - Propulsive Descent		
Engine Thrust (x8)	22500 lbs	100 kN
Load Case 4 - Mars Landing		
Vertical Gs	3 g	3g

Table 2 Scaling and mass variables.

Variable	Baseline Value (English)	Baseline Value (SI)
Total Vehicle Scaling		
X-Direction	1.00	1.00
Y-Direction	1.00	1.00
Z-Direction	1.00	1.00
TPS/Non Structural Mass		
Aft Bulkhead	1500 lbm	680 kg
Cargo Bay Door	1337 lbm	606 kg
FRSI/AFRSI	880 lbm	400 kg
Sirca-15	5480 lbm	2485 kg
Miscellaneous Mass		
MAV	37490 lbm	17000 kg
Landing Gear	2180 lbm	990 kg
LOX Tanks	34640 lbm	15710 kg
CH4 Tanks	11910 lbm	5402 kg
Rocket Motors (Total)	4411 lbm	2000 kg

Table 3 Hypersizer assumptions.

Hypersizer Assumptions	
Safety Factors	1.4 Ultimate, 1.25 Limit
Buckling Knockdown	0.65 OML, 1.0 Otherwise
FEA Load Extraction	0-Sigma (Average)
TPS Deflection Constraint	Radius of Curv. > 10.16 m

Table 4 Variable sensitivity on individual structural property regions.

Names	Total Structures Mass	OML Panels (Aft Bulkhead) Mass	OML Panels (CBD) Mass	Payload Adapter Mass	Tail Ring Mass	Motor Shelves Mass	Ring Frames Mass	Longerons Mass	Substructure (Monoque) Mass	Substructure GSP (Orthogrid) Mass	Substructure Circum. (Monoque) Mass
Input Column											
Scale											
Burst Pressure											
Lateral (g's)											
Axial (g's)											
Max Q											
Engine Thrust (x8)											
Vertical (g's)											
FRSI AFRSI NSM											
Sirca-15 TPS											
Aft Bulkhead NSM											
Tanks (LOX)											
Tanks (CH4)											
Rocket Motors											
MAV											
Landing Gear											

B. Flight Mechanics

For this study, aerocapture was initiated at atmospheric interface (altitude ~125 km) with a hyperbolic excess velocity of 3.758 km/s and an inclination of 90 deg (phase 3 of Fig. 4). The target orbit was a 1-Sol (33973 x 250 km) with an inclination of 90 deg. For this case, the Mid-L/D angle of attack was held constant at 55 deg throughout the atmospheric pass (Note allowing angle of attack modulation would increase the corridor width and potentially reduce the propellant required for aerocapture.) After periapsis, the combination of bank angle and initial flight path angle were used to provide the desired apoapsis while keeping the maximum deceleration below 3.75 Earth g's.

Once the Mid-L/D has reached apoapsis, it maneuvered to raise periapsis to the desired value (phase 4 of Fig. 4). The vehicle then coasted to periapsis, where the apoapsis correction burn was performed to reach the target apoapsis (phase 5 of Fig. 4). This was followed by one to two propulsive maneuvers to remove the longitude of ascending node and the argument of periapsis errors.

The entry trajectory was initiated from a 1-Sol orbit with a deorbit burn of ~16 m/s (phase 7 of Fig. 4), that was sized to meet an entry acceleration limit of 3.75 Earth g's (phase 8 of Fig. 4). The initial entry bank angle was set to control range at pullout. When pullout was reached, the vehicle used bank control to reach the heading alignment phase with the desired velocity, altitude and azimuth. To maintain similarity with realistic flight controllers, bank maneuvers were limited such that the bank angle acceleration was 5 deg/s^2 and the maximum bank rate was 20 deg/s. When the vehicle velocity decreased to 2 km/s, the heading alignment phase commenced, and instead of bank reversals, the bank angle was varied continuously to null out the azimuth error to the landing site at the time of engine initiation. The powered descent phase began when the entry vehicle reached supersonic speeds (Mach ~2-3) and SRP engines were activated (phase 9 of Fig. 4). During this phase aerodynamic forces were not modeled (conservative since drag would decrease propulsion requirements), and SRP thrust levels were set to keep the peak acceleration below the powered descent acceleration limit of 1.5 Earth g's. Descent continued until the vehicle velocity was reduced to 2.5 m/s. At this point, SRP engines were throttled to hold velocity constant for 5 seconds until the vehicle touched down at an altitude of 0 km above the Mars Orbit Laser Altimeter Areoid.

C. Aeroheating Model

High-fidelity predictions of aerothermal environments were made using the Langley Aerothermodynamic Upwind Relaxation Algorithm (LAURA) code (Gnoffo, 1990 and Mazaheri et al., 2013) and the High-Temperature Aerothermodynamic Radiation (HARA) code (Johnston et al., 2008a and Johnston et al., 2008b), which provided convective and radiative heat flux distributions, respectively. Freestream composition was assumed to be 97% CO_2 and 3% N_2 by mass while the flowfield was modeled with an eight-species composition: CO_2, CO, N_2, O_2, NO, C, N, and O. The vehicle surface was modeled as fully-catalytic to homogeneous recombination and having a radiative equilibrium temperature. The HARA radiative heat flux calculations were performed on fully-converged LAURA flowfield calculations using the tangent-slab approach.

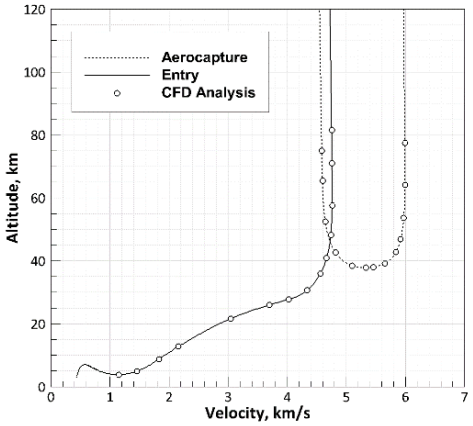

Figure 9 Aerocapture and entry trajectories with points identified for CFD analysis.

Freestream conditions for these Computational Fluid Dynamics (CFD) calculations were taken along simulated aerocapture and entry trajectories, with points selected to fully capture the heat pulses. These trajectories are plotted in Figure 9, along with the individual points identified for CFD analysis. The associated freestream conditions are detailed in Table 5. In all cases, the trimmed vehicle attitude of 55 degrees angle of attack was simulated.

Based upon an assessment of laminar CFD solutions—in particular, observing the ratio of laminar momentum-thickness Reynolds number to boundary-layer edge Mach number—transition to turbulence was predicted to occur early in each trajectory, prior to peak convective heating. Therefore, fully-turbulent CFD solutions were generated at each trajectory point, using the Cebeci-Smith algebraic turbulence model (Cheatwood and Thompson, 1993). Additionally, CFD analyses were focused on obtaining heat flux distributions over the vehicle windward surface. Accurate leeside predictions of convective heat flux require more computationally-complex turbulence models and higher-resolution grids to accurately capture the separated wake flow. Accurate leeside modeling of radiative heat flux would further require the volume grid to be extended into the base flow region to enable application of a full ray-tracing approach, rather than the less computationally-demanding tangent-slab approach. Figure 10 highlights the definition of the windward surface of the modeled vehicle. The CFD volume grid consisted of 48 structured blocks, each with 16 x 16 x 96 cells. Boundary conditions of bilateral symmetry and supersonic outflow were imposed in all cases. Figure 10 depicts the set of symmetry and outflow planes extracted from a volume grid having undergone series solution-based grid adaptations.

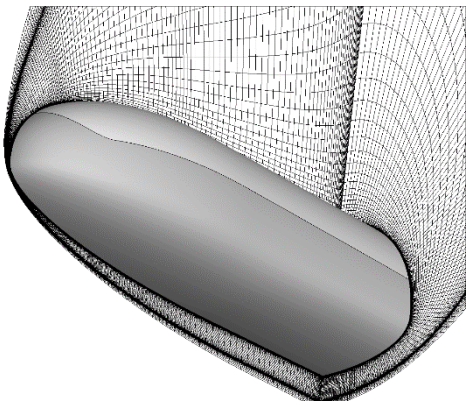

Figure 10 Definition of windward surface, with symmetry and outflow planes of solution-adapted CFD volume grid.

To illustrate the predicted Mid-L/D convective and radiative heating environments, contours of heat flux component magnitudes over the windward surface are shown in Figure 11 for two solutions: one along the aerocapture trajectory (CFD Case A-6) and one along the entry trajectory (CFD Case E-7). These two cases demonstrated the largest total heat flux along their respective trajectories. The heating contours between the two cases are qualitatively similar. Peak convective heat flux generally occurs on the nose region of the vehicle as the flow rapidly expands forward away from the stagnation point and onto the leeside of the body. Turbulence augments the convective heat flux moving aft away from the stagnation point, as the turbulent boundary layer grows more rapidly and entrains higher-energy flow from within the shock layer. The convective heat flux therefore tends to increase toward a second peak at the aft end of the windward surface, with magnitudes here comparable to—or potentially exceeding—those in the nose region.

Table 5 Freestream conditions at CFD analysis cases selected along (a) aerocapture and (b) entry trajectories.

(a) Aerocapture

CFD Case ID	t s	h km	V_∞ km/s	ρ_∞ kg/m^3	T_∞ K
A-1	56	77.5	5.99	1.91e-6	133
A-2	73	64.1	5.99	1.25e-5	139
A-3	89	53.6	5.98	5.27e-5	144
A-4	102	46.8	5.92	1.21e-4	155
A-5	112	42.8	5.84	1.91e-4	162
A-6	128	39.2	5.65	2.90e-4	167
A-7	141	38.0	5.46	3.29e-4	168
A-8	150	37.8	5.33	3.38e-4	169
A-9	167	38.4	5.10	3.14e-4	168
A-10	196	42.7	4.82	1.95e-4	162
A-11	236	52.4	4.65	6.17e-5	146
A-12	274	65.5	4.60	1.03e-5	140
A-13	296	75.0	4.59	2.75e-6	141

(b) Entry

CFD Case ID	t s	h km	V_∞ km/s	ρ_∞ kg/m^3	T_∞ K
E-1	57	81.5	1.06e-6	1.06e-6	128
E-2	72	71.0	4.20e-6	4.20e-6	142
E-3	92	57.5	2.55e-5	2.55e-5	137
E-4	107	48.2	1.06e-4	1.06e-4	134
E-5	120	40.9	2.51e-4	2.51e-4	154
E-6	130	35.9	4.28e-4	4.28e-4	167
E-7	143	30.7	7.19e-4	7.19e-4	181
E-8	157	27.7	9.49e-4	9.49e-4	188
E-9	171	26.0	1.12e-3	1.12e-3	192
E-10	199	21.7	1.65e-3	1.65e-3	200
E-11	236	12.8	3.65e-3	3.65e-3	212
E-12	249	8.77	5.15e-3	5.15e-3	215
E-13	264	4.95	7.18e-3	7.18e-3	219
E-14	280	3.80	7.94e-3	7.94e-3	220

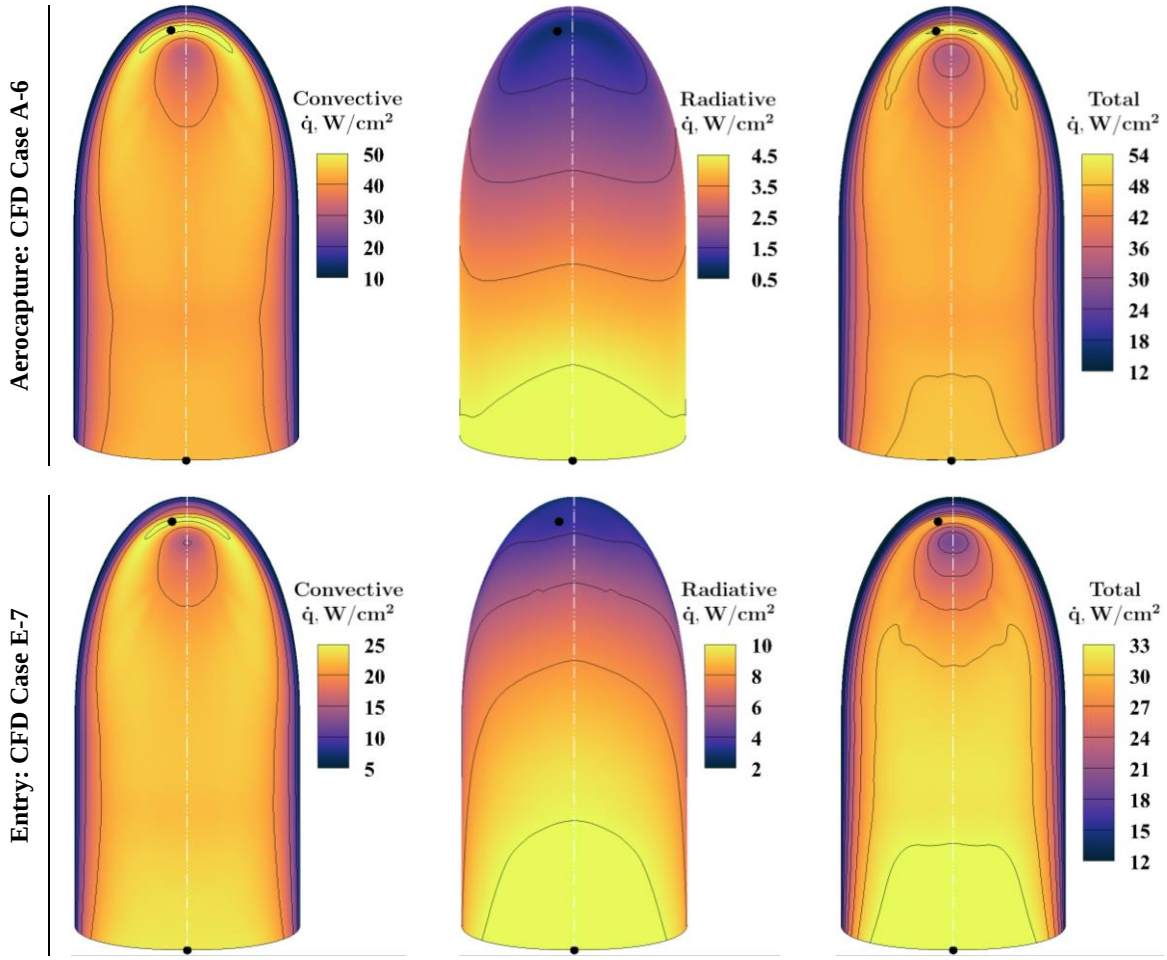

Figure 11 Surface contours of heat-flux component magnitudes for aerocapture and entry CFD cases demonstrating the largest total heat flux: CFD Cases A-6 and E-7.

The radiative heat flux distributions are found to generally increase with axial distance along the body away from the stagnation region as the shock stand-off distance grows monotonically and the vehicle surface is exposed to a larger volume of radiating gas. While the distributions in convective and radiative heat flux components are qualitatively similar between the two cases, the distribution in total heat flux depends on the relative magnitudes of the two contributions. The aerocapture case (CFD Case E-6) heat flux is predominately convective, so the total heat flux distribution is largely defined by that of the convective, except for near the aft end where radiative heat flux attains its largest values and produces a local maximum in total heat flux. Radiative heat flux becomes a much more significant portion of the total heat flux for the entry case (CFD Case E-7). This, combined with a relatively strong level of turbulent augmentation in the aft distribution of convective heat flux, produces a global peak in total heat flux at the aft end of the vehicle. Due to the nature of radiative heating, this peak is much broader in areal coverage than those peaks dominated by locally-high convective heating in the forward nose region.

To compare the relative magnitudes of convective and radiative heat flux along the aerocapture and entry trajectories, two body points were identified corresponding to the local maxima in total heat flux demonstrated in Figure 11. The convective and radiative heat flux at these two body points is plotted in Figure 13 for solutions along the aerocapture trajectory, and in Figure 12 for solutions along the entry trajectory. As seen in Figure 12, the convective heat flux is the dominant contributor to total heating over the entire aerocapture trajectory, at both body points. In contrast, Figure 13 shows that the vehicle experiences the largest radiative heat flux late along the entry trajectory. At this phase in the entry trajectory, the aft body point location experiences a radiative heat flux magnitude that is comparable to that of the convective heat flux. At these slower velocities, the CO_2 molecules are vibrationally excited as they pass through the bow shock, but the resulting post-shock temperatures are not high

enough for dissociation to occur. This large volume of vibrationally excited gas within the shock layer emits infrared radiation that becomes a significant proportion of the total incident heat flux to the vehicle surface. Thus, the radiative heat flux component cannot be neglected, particularly for entry from orbit, in making accurate predictions of total heat load at Mars.

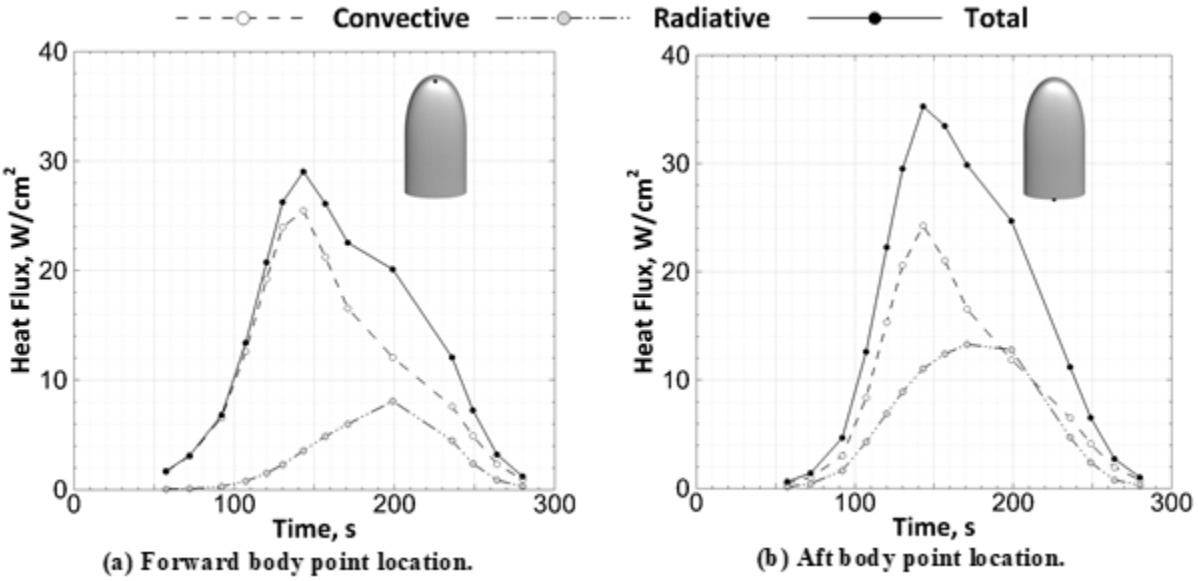

Figure 12 Time histories of heat-flux component magnitudes for all entry trajectory CFD cases, taken at (a) forward and (b) aft body point locations.

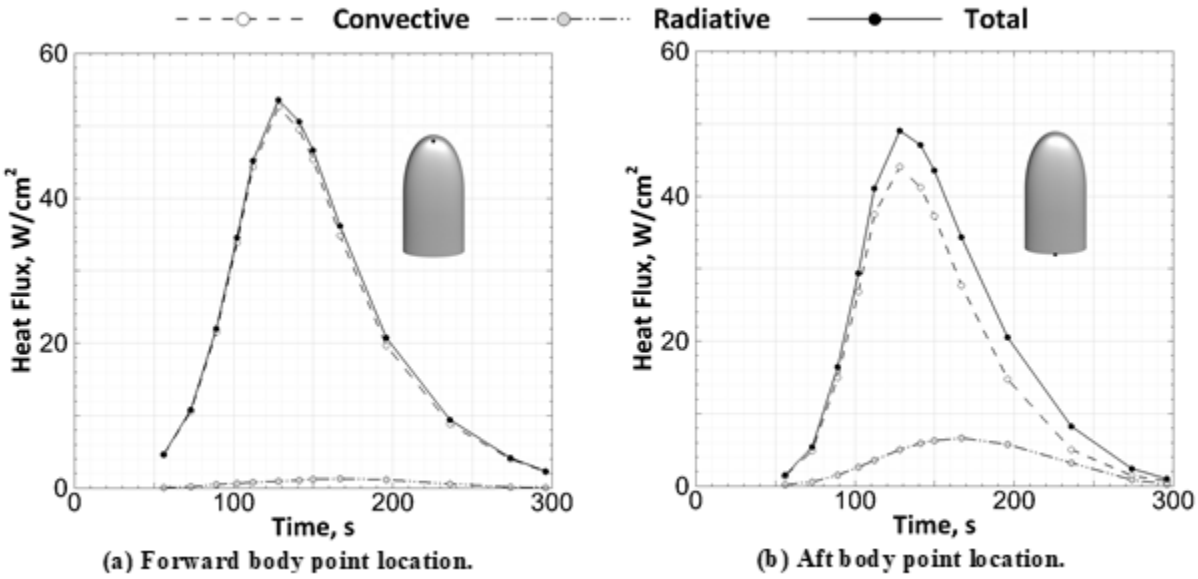

Figure 13 Time histories of heat-flux component magnitudes for all aerocapture trajectory CFD cases, taken at (a) forward and (b) aft body point locations.

To investigate the impact of Mid-L/D vehicle scale on convective and radiative heat flux magnitudes, the vehicle was photographically scaled by factors of $1/\sqrt{2}$ and $\sqrt{2}$ to achieve a halving and doubling of the surface area, respectively. These scaled vehicles were analyzed at the freestream condition corresponding to largest total heat flux among all cases: CFD Case A-6. The relative influence of vehicle scaling on the heat flux components at the forward and aft body locations is shown in Figure 14. Here, heat flux values of the scaled Mid-L/D vehicles have been normalized by those of the unscaled vehicle, and plotted versus the geometric scale factor. The general trends are as expected, with convective heat flux decreasing and radiative heat flux increasing with increasing vehicle scale. The trend in total heat flux magnitude therefore depends on the relative magnitude of these opposing heat flux components, and will thus vary based on freestream condition and location on the vehicle. At the forward body location shown in Figure 12 and Figure 13 convective heat flux is the dominant component of total heat flux. Therefore, the trend in total heat flux follows the same trend that convective heat flux demonstrates scale factor varies. However, at the aft body location, radiative heat flux represents a larger proportion of the total heat flux magnitude. Therefore, the opposing trends in convective and radiative heat flux tend to counteract more and the total heating is less sensitive to varying scale.

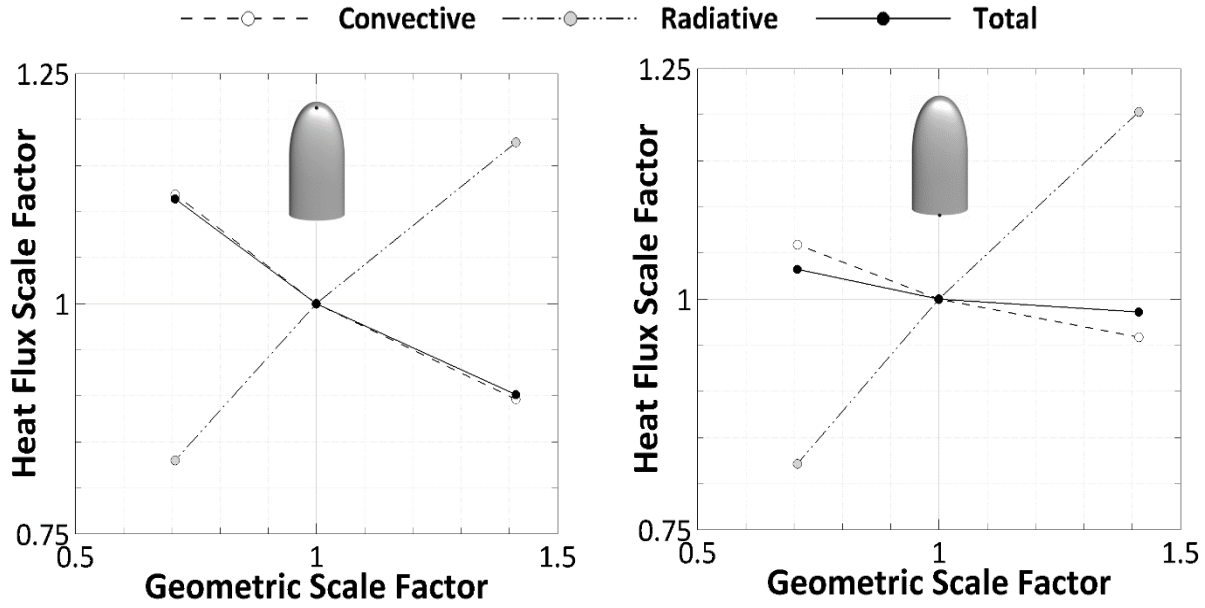

(a) Forward body point location **(b) Aft body point location.**

Figure 14 Impact of geometric scaling on heat-flux component magnitudes, taken at (a) forward and (b) aft body point locations, at aerocapture maximum total heat flux conditions (CFD Case A-6).

D. TPS Model

Aerothermal heating environments are derived for the combined nominal aerocapture and entry trajectories, with a sufficiently long in-orbit cool off period assumed at the end of the aerocapture trajectory and the beginning of the entry trajectory. Peak heat rates occur during the aerocapture phase. For windward acreage, the total heating rate is about 90 W/cm^2. Convective heating is the dominant aeroheating source at peak heating for both aerocapture and entry trajectories. Maximum mission integrated heat load is about 29 kJ/cm^2, and an average windward acreage heat load roughly 20 kJ/cm^2.

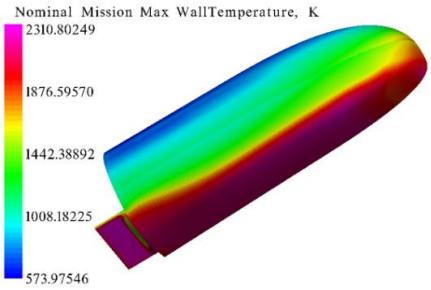

Figure 15 Mission maximum temperatures.

Figure 15 shows the mission maximum surface temperature distribution, which is used as the basis for the TPS material selection and split-line definition. Figure 16 shows the corresponding TPS material split-lines. The leeward TPS consists of Shuttle heritage Felt Reusable Surface Insulation (FRSI) and Advanced FRSI (AFRSI). For the windward surface, Silicon Impregnated Rigid Ceramic Ablator, SIRCA-15 was selected. For the range of heating rates seen, the thermal response of SIRCA is limited to pyrolysis of the injected silicon, with no associated surface recession, and provides roughly 70% heat rate margin based on current aeroheating environments.

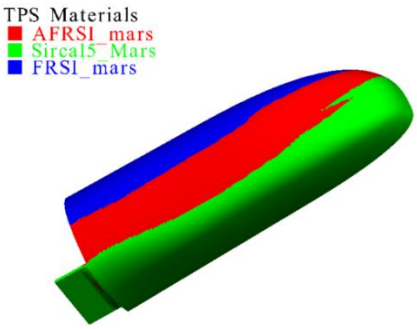

Figure 16 Materials distribution.

TPS material sizing was conducted for the baseline design (McGuire et al., 2004) and using the margins defined in Wright (2009). Since specific aeroheating environments for the body flap due to deflection were not available, the body flap TPS mass was estimated at 200 kg. Areal unit mass of the FRSI and AFRSI are 1.035 and 1.92 kg/m^2, respectively. The flexible blanket systems represent approximately 60% of the total body wetted area, but comprise only roughly 15% of the body TPS mass, with the SIRCA tile mass 85% of the total. The areal unit mass of the SIRCA-15 is 12.06 kg/m^2. The overall body TPS areal unit mass is 5.81 kg/m^2. Total TPS mass, including the assumed body flap TPS mass is 3324.4 kg, with an average areal unit mass of 5.77 kg/m^2.

With the baseline TPS design determined, sensitivity analysis of the TPS material distribution and associated thickness (hence areal mass) was conducted. Variations in total heat load, back-wall structural mass and vehicle scale were addressed. As the design evolves, impact on the TPS mass due to changes in trajectory (hence heating), structural design changes and vehicle size and mass can be quickly assessed with a parametric TPS model.

Figure 17 shows the TPS areal mass sensitivity to relative heat load. FRSI is at minimum gauge thickness, and hence insensitive to heat load (for the range studied). The AFRSI and SIRCA-15 areal masses increase with increasing heat load, with the AFRSI blanket somewhat more sensitive. For a 10% increase in heat load, there is approximately a 3% increase in SIRCA TPS mass. Figure 18 presents TPS areal mass sensitivity to back-wall structural mass. As the back-wall mass increases, the structural heat capacity increases, and the required TPS mass is reduced, with the exception of the FRSI, which is again at minimum gauge.

A study was undertaken to assess the impact of pure photographic scaling on the aerothermal environments and the resulting vehicle TPS mass, using the Co-Optimized Blunt Re-Entry Aero (COBRA) design environment tool (Garcia et al., 2009). Scaling factors of 85%, 67% and 49% were addressed. As the vehicle is scaled down, the corresponding payload mass is computed using a payload density based on the 100% scale. For each scaling factor, the aerodynamic, aerothermodynamic, trajectory performance and mass estimates are recomputed and the vehicle is reclosed in the COBRA framework.

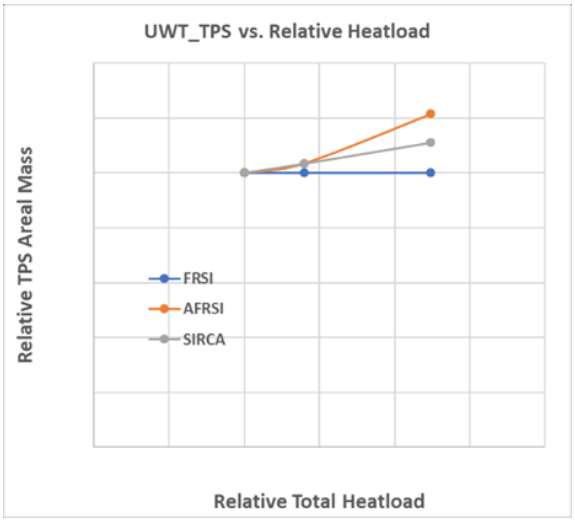

Figure 17 TPS mass vs. relative heat load.

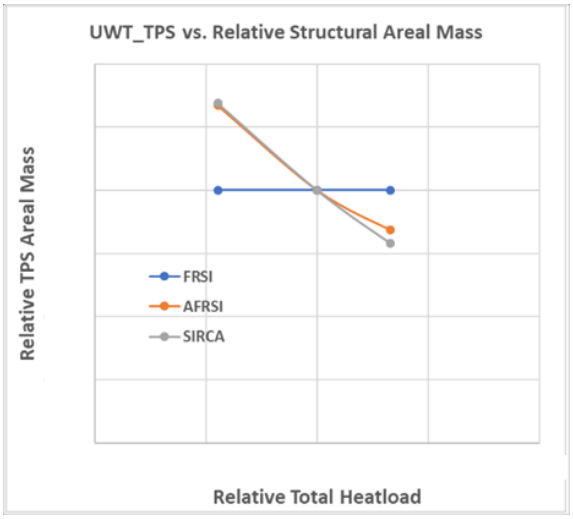

Figure 18 TPS mass vs. back-wall structural mass.

Table 6 summarizes the results of the scaling study, with each vehicle re-sized for the mission. The TPS unit areal mass across the scaling factor range remains essentially constant at 5.80 kg/m^2. Reclosing the vehicle at reduced scale and re-sizing the TPS mass shows a gradual increase in the TPS dry mass fraction, approximately 12% at full scale, rising to 15% at roughly 50% scale.

Table 6 Photographic scaling summary results.

Scale Factor	Ballistic Coeff (kg/m^2)	TPS Mass (kg)	Empty Mass (kg)	Payload Mass (kg)	Arrival Mass (kg)
100%	351	3424	28700	20000	63250
85%	310	2481	19060	12285	40500
67%	263	1506	10660	6000	21400
49%	220	803	5100	2350	9575

Both the heat rates and integrated heat load decrease as the vehicle is photographically scaled down. The windward SIRCA wetted area decreases with lower vehicle size due to lower acreage heat rates, while the AFRSI area increases due to less required surface area for the higher temperature capable SIRCA system, as shown in Figure 19. The impact of vehicle size is incorporated into the TPS Mass Estimating Relationship (MER) presented below. The relative TPS areal mass versus vehicle scale is presented in Figure 20, with both blanket TPS systems areal masses remaining essentially constant with vehicle scale. This trend occurs because both the FRSI and the AFRSI are at or very close to minimum gauge thickness; hence, their areal mass is virtually independent as vehicle scale. With TPS thickness and areal mass decreasing with lower heat load, the unit areal mass for the SIRCA system reduces as the vehicle scale is reduced, reflected in the heat load trend with vehicle scale presented in Figure 20. This trend is also included in the TPS MER equations presented in Figure 21.

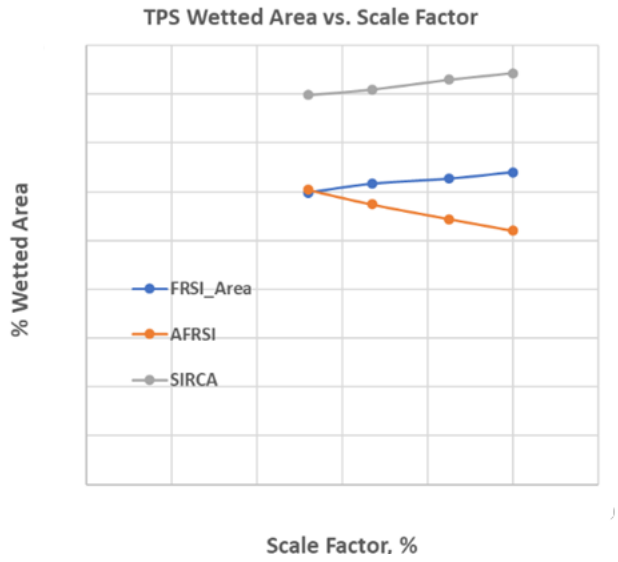

Figure 19 TPS material split line vs. scale.

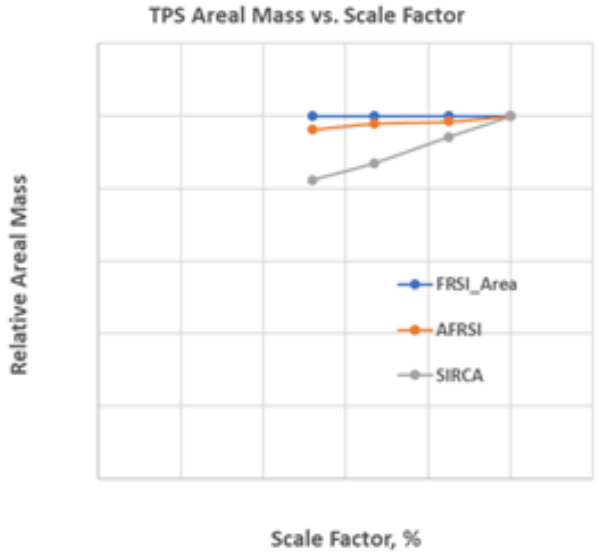

Figure 20 TPS areal mass vs. scale.

Total_TPS_Mass = Windward_TPS_Mass + Leeward_TPS_Mass

$$= L_{BODY}^{2} * k_{SWET} * (\%A_{SIRCA} * UWT_{SIRCA} * (HL'/HL\_ref)^{\alpha_{SIRCA}} * (UWT_{STR}/10.3)^{\beta_{SIRCA}} + \%A_{AFRSI} * UWT_{AFRSI} * (HL'/HL\_ref)^{\alpha_{AFRSI}} * (UWT_{STR}/10.3)^{\beta_{AFRSI}} + \%A_{FRSI} * UWT_{FRSI})$$

Where:

L_{BODY} = Vehicle Body Length, m

$k_{SWET} = 1.469$

$\%A_{SIRCA} = 0.4205*(L_{BODY}/19.8)^{0.0842}$

$\%A_{AFRSI} = 0.2613*(L_{BODY}/19.8)^{-0.226}$

$\%A_{FRSI} = 0.3196*(L_{BODY}/19.8)^{0.0999}$

$UWT_{SIRCA} = 12.06*(L_{BODY}/19.8)^{0.2988}$ kg/m^2

$UWT_{AFRSI} = 1.923*(L_{BODY}/19.8)^{0.0539}$ kg/m^2

$UWT_{FRSI} = 1.034$ kg/m^2

$\alpha_{SIRCA} = 0.2185$

$\beta_{SIRCA} = -0.525$

$\alpha_{AFRSI} = 0.375$ and $\beta_{AFRSI} = -0.475$

HL = integrated Heat Load along new acerocapture + entry trajectory using Heat Rate Indicator Correlation, J/cm^2

$HL' = HL*(L_{BODY}/19.8)^{0.5239}$

HL_ref = integrated Heat Load along reference acerocapture + entry = 15797 J/cm^2

Note: TPS mass model does not include any weight growth allowance (WGA), nor any project manager level margins.

Figure 21 TPS MER equations.

E. Lander Model

The Exploration Architecture Model for the IN-space and Earth-to-orbit modeling (EXAMINE) tool, developed in-house at NASA Langley (Komar et al., 2008), was used to develop the parametric mass estimates of the Mid-L/D lander. To model the Mid-L/D, EXAMINE subsystem models for structures and mechanisms, TPS, main propulsion system (MPS) storage and feed, RCS storage and feed, main engines and RCS thrusters, power, avionics, and thermal control were used to represent the functional design. EXAMINE's Transportation System Requirements (TSR) model was used to model the concept of operations and mission events from Earth departure to Mars landing. The TSR model predicts propellant requirements for the vehicle's MPS and RCS as a function of the event mass, engine specific impulse, and required event performance (ΔV); and manages the integrated sizing of the functional subsystems. Table 7 shows events and nominal ΔVs for modeling the Mid-L/D concept.

Table 7 Events and ΔV requirements for the Mid-L/D vehicle.

Mission Event	MPS ΔV (m/s)	RCS ΔV (m/s)
Earth Orbit Rendezvous and Docking with SEP	---	45
Earth Orbit Stage Separation from SEP	---	10
Aerocapture Targeting	---	30
Aerocapture Maneuvering	---	30
Post-Aerocapture Periapsis Raise	---	15
Post-Aerocapture Apoapsis Cleanup	---	10
Mars Orbit Loiter	---	20
Mars Orbit Rendezvous and Docking with Crew Vehicle	---	10
Mars Orbit Stage Separation from Crew Vehicle	---	20
Mars Descent Orbit Insertion	---	30
Powered Descent and Landing	688	30

Subsections III.A and III.D describe the modeling techniques for the primary structure, mechanisms and TPS subsystems. Data from these models, including structural surface areas and unit masses, were passed to EXAMINE's integrated mass model. Landing legs were modeled as 1.64% of the landed mass, while secondary structure was assumed 20% of the vehicle dry mass not including the TPS.

The liquid oxygen (LOX) and liquid methane (LCH_4) propellants for main propulsion system (MPS) and the RCS are stored in the aluminum tanks (two for each propellant) at 50 psia. An advanced cryogenic propellant management technology—multi layer insulation (MLI) plus single-stage cryo-cooling system—is used to eliminate boiloff and provide pressurization and control. In addition to the mission required usable propellants, tank sizing includes 4% reserve propellant (including 1% flight performance reserve and 3% for tank venting and engine startup/shutdown), 1.5% for residual propellant, and 3% for ullage gases. The MPS has eight pump-fed engines, used solely for SRP, with each operating at 2000 psia chamber pressure and a mixture ratio of 3.2. The engines each deliver 100 kN of thrust at 360 sec of specific impulse, with each engine having a thrust-to-mass ratio of 51.

For the RCS system, a set of accumulator bottles, sized to contain propellants for the large entry RCS control requirement, are recharged for each RCS event to 300 psia by pumping the needed RCS propellant from the MPS to the accumulators. The RCS has 4 sets of 6 pressure-fed thrusters, with 3 producing 100 lbf (445 N) and 3 producing 1000 lbf (4448 N). The 100-lbf (445 N) thrusters provide on-orbit attitude and translational control, while the 1000 lbf (4448 N) thrusters are used for entry attitude control. Each thruster operates at a chamber pressure of 250 psia, a mixture ratio of 3, and an area ratio of 25, delivering a vacuum specific impulse of 330 sec.

Several power systems are used on the vehicle. One set of photovoltaic arrays support interplanetary coast and are jettisoned prior to aerocapture. A second set of photovoltaic arrays support pre-entry phases and are jettisoned prior to de-orbit. These arrays are sized for 12 kW for a 5-year operation with 5% degradation per year assuming mass specific power of 150 W/kg and areal specific power of 250 W/m^2 at beginning-of-life. Lithium-ion batteries support pre-deployment of arrays, during the aerocapture maneuver, and for de-orbit/entry, terminal landing and post-landing operations. Nine were batteries sized for 8 hours to deliver 5 kW total (40 kW-hrs) assuming a specific

energy of 125 W-hr/kg. Solid-oxide fuel cells (SOFC) are used for post-landing up to 3.75 days to power the cooling and avionics systems until ground power is connected. Four cells are sized for 10 kW peak and 5 kW average power assuming a specific mass of 16.4 kg/kW produced and 1.6074 kW-hr/kg O_2/CH_4 consumed. The power management and distribution (PMAD) system is 95% efficiency and sized to handle 18 kW peak power load assuming a sizing factor of 15 kg/kW.

Additional subsystems include the thermal control system (TCS) and avionics. The TCS delivers 18 kW of thermal heat, collected primarily from the cryo-cooling and power systems, to the outer bay mounted radiators sized with a specific mass of 25 kg/kW. The avionics systems are derived from NASA's Altair lunar lander project and include components supporting command and data handling, communications and tracking, and guidance, navigation and control. An average mass growth allowance of 21.8% is included in the mass estimates.

F. Aerodynamics

The aerodynamic model is a database constructed from several sources, including Direct Simulation Monte Carlo (DSMC), CFD, wind tunnels, and ballistics range data (Cerimele et al. 2017 and Sostaric et al. 2019). The database covers free-molecular, hypersonic, supersonic, and subsonic regimes. The database has been integrated into the flight mechanics code, Program to Optimize Simulated Trajectories II (Brauer et al. 1977).

IV. Alternative Structures Concepts

Two alternative structural concepts were considered: Integrated Composite Stiffener Structure (ICoSS) (Kellas 2014) to replace the honeycomb sandwich OML panels, longerons, and ringframes; or hot structure with fibrous insulation backing to replace the windward honeycomb sandwich OML panels and TPS. Both alternatives will be discussed in the paragraphs that follow.

1. ICoSS

Unpublished preliminary analysis performed by Collier Research indicated that using ICoSS would reduce structural weight by 40% for the 2018 Systems Analysis of Planetary EDL (SAPE) baseline model, which would lead to an 11% reduction in vehicle weight. It was decided to further investigate ICoSS with the HyperSizer structural sizing script described in section III.A. As shown in Figure 22, ICoSS consists of a composite skin with intersecting foam filled hat stiffeners. The skin is laid up on a mold, forming a smooth outer surface that conforms to complex curvatures. A machined foam core is then positioned on the inner surface of the skin and is used to define the hat stiffener position and shape. Strips of composite plies may be placed at the crown and base of the foam, and integrating textile composite plies are draped over the foam and crown plies. The entire panel is then co-cured providing excellent strength and damage tolerance. As an example, drop tests of a carrier structure exhibited minimal damage after testing (Kellas 2017). Other structural benefits of the ICoSS approach are: continuous load paths through the crown and base plies; high structural efficiency hat stiffeners; plies can be tailored going around the base, web, and crown of the hat stiffener; and the foam potentially stabilizes the web against local buckling. If used to replace ringframes and longerons, the ICoSS design would essentially take on the form of a foam filled box beam. For use with brittle TPS, the pockets between hat stiffeners can be filled with foam to reduce curvature between stiffeners. In addition, the coefficient of thermal expansion (CTE) range of composites that would typically be used for ICoSS are in the same range as many TPS materials.

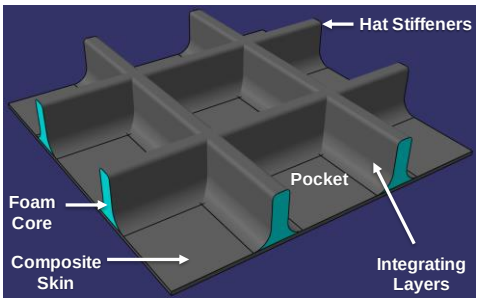

Figure 22 Typical ICoSS panel.

There are no exact concept definitions for the ICoSS design in HyperSizer, but there is a concept definition with a hat stiffener running in one direction attached to a foam sandwich skin. By using a multi-step process, it was possible to first run an orthogrid concept to size the skin and generate stiffener spacing and panel bending requirements, and then push this information to hat stiffener concepts aligned in the longitudinal and transverse directions to size the hat stiffeners. This approach was sufficient for a preliminary analysis but made it impossible

to account for stresses at the base of the hat stiffeners or transverse failure interactions. Another limitation was encountered due to the foam weight being absent from the HyperSizer optimization logic, which at times resulted in non-optimum solutions.

ICoSS was analyzed as a replacement for both the OML panels and the ringframe and longeron "T" beams using the baseline model. Weights are compared with the baseline design in Table **8**. Using ICoSS for the OML panels resulted in a weight savings of 296 kg, entirely from the aft region. Percentage weight savings were more dramatic for the ringframe and longeron assemblies, where in both cases the assembly weight was reduced by more than 50%. It is likely that weights can be reduced by further composite layup optimization. Also, as noted previously, since the hat foam weight is not included in the HyperSizer optimization, the ICoSS weights reported may be higher than the optimum ICoSS weight.

Table 8 ICoSS Panel weight comparison.

Concept	Assembly Weights (kg)		
	Panels	Ringframes	Longerons
Baseline	3120	606	549
ICoSS	2824	273	229

Although HyperSizer clearly indicates that there are benefits to using ICoSS, the analysis limitations make it difficult to complete the study without either modifications to HyperSizer or additional studies performed outside of HyperSizer. It is recommended that structural modeling and testing be performed on ICoSS panels subjected to typical vehicle loads. From this data, the HyperSizer results can be verified or the data can be used to define a sizing approach outside of HyperSizer.

2. Hot Structure Concept

The hot structure concept replaces the windward TPS and honeycomb sandwich panels with an Advanced Carbon-Carbon-6 (ACC-6) hot structure panel, backed with fibrous insulation. The potential advantage of this approach is that, by carrying the entry loads, the hot structure panel allows high efficiency fibrous insulation to be used as a backing material, such as Opacified Fibrous Insulations (OFI), with Nextel fabric used to bag the insulation. In addition, the hot structure OML will experience minimal recession during entry, resulting in a stable, smooth aerodynamic surface. Figure 23 shows a potential hot structure cross section.

There are several challenges that arise when hot structures are attached to ringframes and longerons. Structural materials that can go to high temperatures tend to be brittle and have poor through the thickness strength, which makes spanning a panel between frames difficult. In addition, the attachment to the ringframes or longerons will produce a heat short that will raise their temperature approaching the temperature as the hot structure. This will require that the substructure also be made of high temperature materials, which are not likely to be as structurally efficient as traditional structural materials. It is possible that substructure temperatures could be reduced by introducing stand-offs between the hot structure and the substructure, similar to ideas shown in Kochendorfer (2001) and Blosser et al. (2004), but this would introduce further complexity and increase weight.

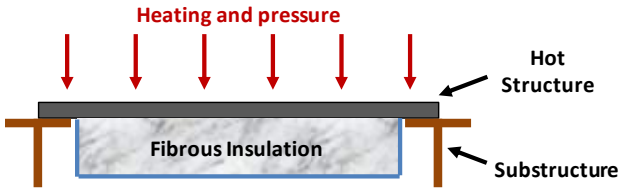

Figure 23 Hot structure schematic.

Preliminary analysis was performed assuming that the hot structure attaches directly to the substructure, and neglecting the effect of thermal growth and thermal gradients. The purpose of the analysis was to estimate the structural weight gain due to using ACC-6 monocoque panels spanning the ringframes and longerons instead of the baseline honeycomb sandwich concept. Once this weight gain is known, it will give a target for understanding how efficient the fibrous insulation will have to be in order to save weight. Results are graphed in Figure 24 as "ACC-Mono", along with the Sirca-15 TPS weight at a vehicle scale of 1.0. Clearly, since the weight gain associated with using monocoque ACC at a scale of 1.0 is almost equal to the windward TPS weight, there could be no benefit to using monocoque ACC at a scale of 1.0, and probably not at smaller scales, since the insulation weight would have to be negligible. Further analyses were conducted assuming that stiffeners are added to the backside of the ACC panel, which was approximated with two different orthogrid concepts. The first assumed an orthogrid pattern cut out of ACC panels limited to 2.3 inches in thickness, referred to as "ACC-Thin Ortho" in Figure 24. The second concept assumes that there is no limit to the orthogrid stiffener heights, and is referred to as "ACC-Thick Ortho".

Adding stiffeners on the back of the ACC panel clearly helps for room temperature analysis, with ACC-Thick Ortho showing only a 954 kg weight gain at a vehicle scale of 1.0. If the thermal efficiency of the fibrous insulation is significantly better than Sirca-15, there is room for weight savings. There is a clear decline in return for allowing the stiffened ACC panel to exceed 2.3 inches total thickness. In addition, the weight gain associated with using ACC is reduced as the vehicle scale is reduced, since the span between ringframes and longerons is reduced, making it easier for the ACC panels to satisfy curvature constraints and resist buckling. It should however be cautioned that ACC possesses weak through the thickness strength and attachment of stiffeners or machining out an orthogrid shape would not be trivial or inexpensive. In addition, weight is likely to be added as the design is matured. A logical forward path for this design would be to perform a preliminary insulation sizing at several vehicle scales, and compare the TPS weight savings to the hot structure weight gains. If there is potential for significant weight savings, the feasibility of making stiffened hot structure panels should be investigated further.

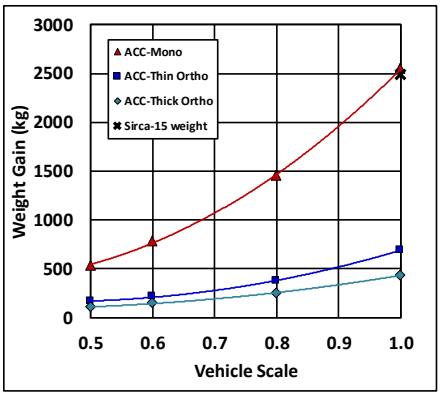

Figure 24 Structural panel weight gain from ACC concepts.

V. Results

The baseline Mid-L/D entry system is capable of landing 20-t payload on the Mars surface. The nominal vehicle trajectory was designed to limit the maximum deceleration loads to three Earth g's (3.75 Earth g's for design dispersion), not overloading the de-conditioned crew. Margins for heat fluxes were 40% for convective and 50% for radiative. The vehicle's arrival C_∞ is 3.758 km/s (6.2 km/s relative velocity at 90° inclination) and with a captured parking orbit of 1-Sol.

It took four iterations to converge to a target payload of 20 t. Figure 25 shows the mass breakdown for the Mid-L/D baseline entry system. Figure 26 shows the environments for aerocapture and entry trajectories. Figure 27 shows mass losses during each phase of the mission. There are ten losses for the attitude control systems (ACS). The largest ACS burn is for the powered descent and landing.

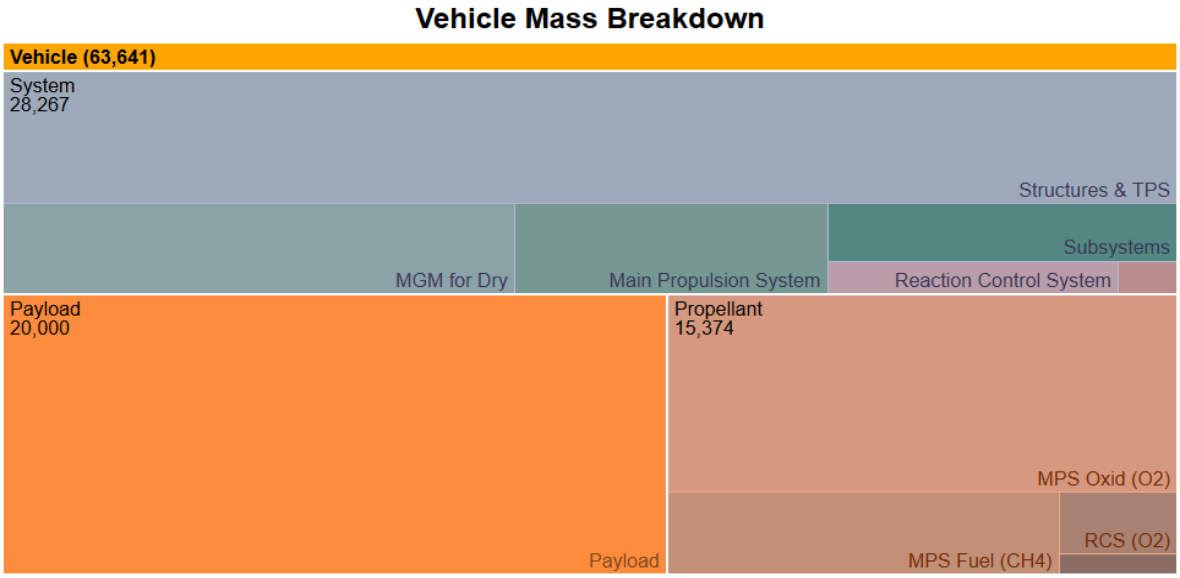

Figure 25 Baseline Mid-L/D mass breakdown (numbers are masses in kg).

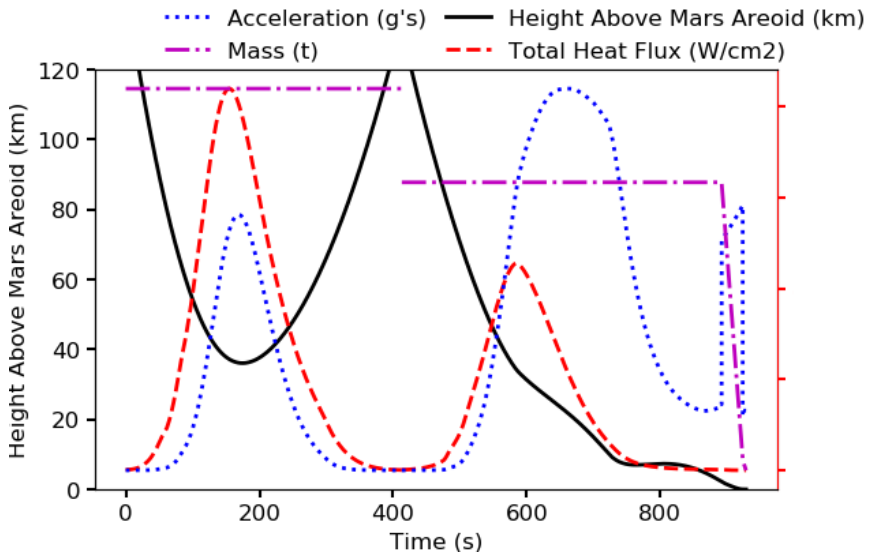

Figure 26 Baseline Mid-L/D trajectory environment.

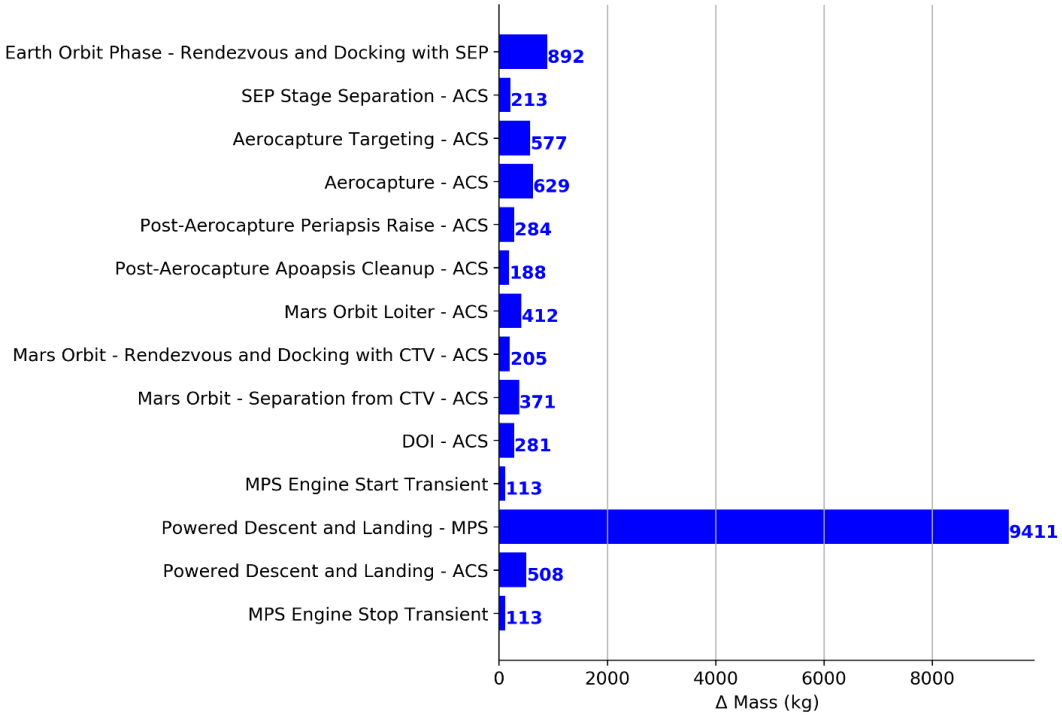

Figure 27 Baseline Mid-L/D mass losses during each phase of the mission.

A. System-Level Sensitivity Analysis

The baseline system includes many assumptions such as margins, arrival state, ConOps options, parking orbit, physical dimensions, and technology concepts. Changes in one of the assumptions could have a profound impact on the overall system. Through sensitivity analysis, it is possible to quantify the systems-level impact of assumptions and various parameters. Systems-level sensitives expose major design drivers and highlight the importance of each assumption for a given design.

To compare sensitivities across many inputs and output parameters, the sensitivities are normalized as percent changes in the outputs per percent changes in the inputs:

$$\text{Sensitivity} = \frac{\frac{f(x+\Delta x)-f(x)}{f(x)}}{\frac{\Delta x}{x}} = \frac{\%\ \text{Change in Output}}{\%\ \text{Change in Input}} \quad (1)$$

The term x is an input parameter (e.g., heat flux margin) and $f(x)$ is an output parameter (e.g., system mass). The value for Δx is selected so we can calculate a meaningful sensitivity. For example, using 10% for Δx is too large for engine Isp but appropriate for aeroshell ballistic coefficient. The sensitivity for discrete parameters such as ConOps is treated similarly except $\Delta x/x$ is set to 1; sensitivity is then reduced to percent change in the output. Sensitivities are calculated for a specific design point, and they will change as the design changes. Sensitivities can be used to calculate uncertainties using first order methods.

For a selected set of input and output parameters, Table 9 shows the system-level sensitivity matrix for the baseline Mid-L/D entry system. The first column lists input parameters. The top two rows are names and values of the baseline output parameters. The remaining rows and columns show system-level sensitivities. The negative and positives values are in red and blue, respectively. The intensity of colors indicates the magnitude of sensitivity. Rows in the sensitivity matrix can represent technology push. For example, an advanced structural concept for improving MDM can be represented as *MDM Mass Growth Allowance*. The columns can represent technology pull. For example, technology drivers to reduce the TMI mass are improvements in payload and Isp.

Table 9 System-level sensitivities.

		Output Parameters										
		Gear Ratio	Total Mass (kg)	TMI Mass (kg)	AC Mass (kg)	DeOrbit Mass (kg)	MDM Inert Mass (kg)	Usable Prop Mass (kg)	AC Max Heat Flux (W/m2)	EDL Max Heat Flux (W/m2)	AC Heat Load (J/m2)	EDL Heat Load (J/m2)
	Baseline	3.182	63640	62535	61958	59869	29442	14197	839845	455197	1.14E+08	6.27E+07
Input Parameters	Payload Mass (kg)											
	BC Scale											
	Main Engine Cant Angle (deg)											
	AC Max G											
	Terminal Delta V Correction (%)											
	MDM Mass Growth Allowance											
	Convective Heating Margin (%)											
	Radiative Heating Margin (%)											
	TPS Margin (%)											
	Secondary Structure (%)											
	Landing Legs (%)											
	Windward TPS Type (SIRCA->PICA)											
	Hyperbolic Velocity (m/s)											
	Inclination (deg)											
	MDM MPE Isp Factor											
	MDM RCE Isp Factor											
	MDM MPE Thrust per Engine (kN)											
	MDM MPS Tank Pressure (psia)											

B. Tradespace Exploration

Tradespace exploration examines a wide range of system parameters and compares possible design options. This examination enables trades associated with system parameters and its resulting cost and benefit metrics. It also provides the decision maker with the design information that accounts for the impact of multiple parameters and their interdependent output parameters.

Tradespace studies were performed for several input parameters. Figure 28 shows a sample tradespace for payload mass (y-axis) and vehicle length (x-axis). The contour plots are based on 147 individual designs that were

converged and have a consistent mass breakdown. The contour lines show TMI mass and gear ratio. The gear ratio is a surrogate for entry system efficiency, and it is defined as arrival mass divided by payload mass. The gear ratio is lower for higher payload (larger systems are more mass efficient). There is no optimum design for a given vehicle length.

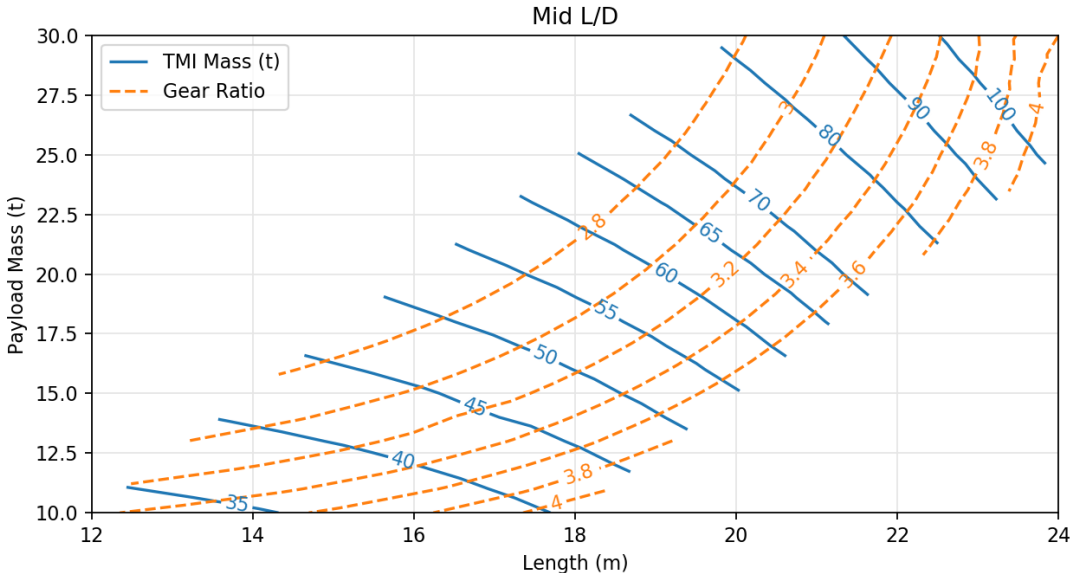

Figure 28 Mid-L/D tradespace for payload mass and vehicle length.

VI. Summary Remarks

This paper provides a data-driven and physics-based systems analysis and tradespace exploration for a human Mars entry system using a Mid-L/D concept. Two alternative structural concepts have also been discussed. The paper includes an overview of the parametric mass models. Baseline results are presented and discussed. A systems level sensitivity analysis is presented. The results of tradespace explorations also provided. The Integrated Composite Stiffener Structure (ICoSS) structural concept offers significant weight savings and should be pursued further. The Hot structure TPS structural concept has many structural challenges, which are partially alleviated by using smaller frame spacing. However, if it can be shown that weight savings from using fibrous insulation are greater than the added structural weight this design could be worth pursuing.

Acknowledgments

The authors would like to acknowledge August Noevere (Collier R&D) for his recommendations for modeling the ICoSS design in HyperSizer, Paul Tartabini and Dick Powell for help with flight mechanics, and Lance Proctor for guidance on the structural model. The authors would like to thank members of the EDLAS Team from NASA Ames, Langley, JSC, and MSFC.

References

Blosser, M. L., Poteet, C. C., Chen, R. R., Dorsey, J. T., Schmidt, I. H., Bird, R. K., and Wurster, K. E. (2004). "Development of Advanced Metallic Thermal-Protection-System Prototype Hardware," Journal of Spacecraft and Rockets, Vol. 41, No. 2, March-April 2004.
https://doi.org/10.2514/1.9179

Brauer, G. L., Petersen, F. M., Cornick, D. E., Stevenson, R., Olson, D. W. (1994) "Capabilities and Applications of the Program to Optimize Simulated Trajectories (POST)," LAR-14869, LAR-14871, Feb. 1994.

Calderon, D., Sostaric, R., Gaytan, C., Newton, H., Amar, J, and Wiens, Z. (2020) "Manifest Packaging and Mass Optimization of a Mars Entry Vehicle" – Abstract Accepted SciTech2020.

Cassell, A., Brivkalns, C., Garcia, J., Bowles, J., Kinney, D., Yount, B., McGuire, K., Wercinski, P., Cianciolo, A., Polsgrove, T. (2017) "Human Mars Mission Design Study Utilizing the Adaptive Deployable Entry and Placement Technology," IEEE Aerospace Conference, Big Sky, MT 2017.
https://doi.org/10.1109/aero.2017.7943585

Cerimele, C., Robertson, E., Sostaric, R., Campbell, C., Robinson, P., Hershey, M., Stachowiak, S., Matz, D., Braden, E., Johnson, B., Garcia, J., Bowles, J., Kinney, D. (2017) "A Rigid Mid Lift-to-Drag Ratio Approach to Human Mars Entry, Descent, and Landing" AIAA SciTech 2017 Grapevine TX 2017.
https://doi.org/10.2514/6.2017-1898

Cheatwood, F. M., and Thompson, R. A. (1993) "The Addition of Algebraic Turbulence Modeling to Program LAURA," NASA TM-107758, April 1993.
http://hdl.handle.net/2060/19930018061

Chen, Y. K. and Milos, F. S. (1999) "Ablation and Thermal Response Program for Spacecraft Heatshield Analysis," Journal of Spacecraft and Rockets, Vol. 36, No. 3, 1999, pp. 475-483.
https://doi.org/10.2514/2.3469

Drake, B. G., "Human Exploration of Mars Design Reference Architecture 5.0" (2009) NASA/SP–2009–566, July 2009.
http://hdl.handle.net/2060/20160003093

Drake, B. G. and Watts, K. D. (2014) "Human Exploration of Mars Design Reference Architecture 5.0, Addendum #2," NASA/SP–2009-566-ADD2, March 2014.
http://hdl.handle.net/2060/20160003093

Dwyer Ciancolo, A. M., Davis, J. L., Komar, D. R., Munk, M. M., Samareh, J. A., Williams-Byrd, J. A., Zang, T. A., Powell, R. W., Shidner, J. D., Stanley, D. O., Wilhite, A. W., Kinney, D. J., McGuire, M. K., Arnold, J. O., Howard, A. R., Sostaric, R. R., Studak, J. W., Zumwalt, C. H., Llama, E. G., Casoliva, J., Ivanov, M. C., Clark, I., and Sengupta, A. (2010) "Entry, Descent and Landing Systems Analysis Study: Phase 1 Report, July 2010, NASA/TM-2010-216720.
http://hdl.handle.net/2060/20100026676

Dwyer Cianciolo, A. and Polsgrove, T. (2016) "Human Mars Entry, Descent and Landing Architectures Study Overview," AIAA SPACE 2016; 13-16 Sep. 2016; Long Beach, CA.
https://doi.org/10.2514/6.2018-5190

Garcia, J. A., Brown, J. L., Kinney, D. J., Bowles, J. V., Huynh, L. C., Jiang, X. J., Lau, E., and Dupzyk, I. C. (2010) "Co-Optimization of Mid Lift to Drag Vehicle Concepts for Mars Atmospheric Entry," AIAA-2010-5052.
https://doi.org/10.2514/6.2010-5052

Gnoffo, P. A. (1990) "An Upwind-Biased, Point-Implicit Algorithm for Viscous, Compressible Perfect-Gas Flows," NASA TP-2953, Feb. 1990.
http://hdl.handle.net/2060/19900007726

Ivanov, M. C., Blood, E. M., Cook, B. T., Giersch, L. R., Grover, M. R., Jakobowski, J. K., Rivellini, T. P., Su, R. P., Samareh, J. A., Zang, T. A., Winski, R. G., Olds, A. D., and Kinney, D. J. (2011) "Entry, Descent and Landing Systems Analysis Study: Phase 2 Report on Mars Science Laboratory Improvement," January 2011, NASA/TM-2011-216988.

Johnston, C. O., Hollis, B. R., and Sutton, K. (2008a) "Non-Boltzmann Modeling for Air Shock Layers at Lunar Return Conditions," Journal of Spacecraft and Rockets, Vol. 45, No. 5, 2008, pp. 879-890.

https://doi.org/10.2514/1.33006

Johnston, C. O., Hollis, B. R., and Sutton, K. (2008b) "Spectrum Modeling for Air Shock-layer Radiation at Lunar-Return Conditions," Journal of Spacecraft and Rockets, Vol. 45, No. 5, 2008, pp. 865-878.
https://doi.org/10.2514/1.33004

Kellas, S. (2016) "Integrated Composite Stiffeners Structure (ICoSS) Concept for Planetary Entry Vehicles," AIAA 2016-1718, 57th AIAA / ASCE / AHS / ASC Structures, Structural Dynamics, and Materials Conference, San Diego, CA, January 2016.
https://doi.org/10.2514/6.2016-1718

Kellas, S. (2017) "Passive Earth Entry Vehicle Landing Test," IEEE Aerospace Conference, Big Sky, MT, March 4-11, 2017.
https://doi.org/10.1109/AERO.2017.7943744

Kochendorfer, R. (2001) "Ceramic Matrix Composites – From Space to Earth: The Move From Prototype to Serial Production," Ceramic Engineering & Science Proceedings, Volume 22, Issue 3, 2001.
https://doi.org/10.1002/9780470294680.ch2

Komar, D. R., Hoffman, J., and Olds, A. (2008) "Framework for the Parametric System Modeling of Space Exploration Architectures," AIAA-2008-7845, 2008.
https://doi.org/10.2514/6.2008-7845

Langston, S. L., Lang, C. G., Samareh, J. A., and Daryabeigi, K. (2016) "Optimization of a Hot Structure Aeroshell and Nose Cap for Mars Atmospheric Entry," AIAA-2016-5594.
https://doi.org/10.2514/6.2016-5594

Lillard, R., Olejniczak, J., Polsgrove, T., Cianciolo, A., Munk, M., Whetsel, C., Drake, B. (2017) "Human Mars EDL Pathfinder Study: Assessment of Technology Development Gaps and Mitigations," IEEE Aerospace Conference, Big Sky, MT 2017.
https://doi.org/10.1109/aero.2017.7943587

McGuire M. K., Bowles J., Yang L., Kinney D., Roberts C. (2004) "TPS Selection and Sizing Tool Implemented in an Advanced Engineering Environment," AIAA-2004-342, 42nd AIAA Aerospace Sciences Meeting and Exhibit, Reno NV, Jan. 2004
https://doi.org/10.2514/6.2014-0342

Mazaheri, A., Gnoffo, P. A., Johnston, C. O., Kleb, B. (2013) "LAURA Users Manual: 5.5-65135," NASA/TM-2013-217800.
http://hdl.handle.net/2060/20130009520

Percy, T. K., Polsgrove, T., Sutherlin, S., and Dwyer Cianciolo, A. (2018) "Human Mars Entry, Descent and Landing Architecture Study: Descent Systems," AIAA-2018-5193.
https://doi.org/10.2514/6.2018-5193

Portree, D. S. (2001) "Humans to Mars: Fifty Years of Mission Planning, 1950-2000, NAS Monographs in Aerospace History Series, Number 21, February 2001.
https://history.nasa.gov/monograph21.pdf

Polsgrove, Tara P., Chapman, J., Sutherlin, S., Taylor, B., Fabisinski, L., Collins, T., Cianciolo, A., Samareh J., Robertson, E., Studak, W., Vitalpur, S., Lee, A., Rakow, G. (2016) "Human Mars Lander Design for NASA's Evolvable Mars Campaign," IEEE Aerospace Conference, Big Sky, MT, March 2016.
https://doi.org/10.1109/aero.2016.7500778

Polsgrove, Tara P., Thomas, H. D., Dwyer Cianciolo, A., Collins, and Samareh J. (2017) "Mission and Design Sensitivities for Human Mars Landers Using Hypersonic Inflatable Aerodynamic Decelerators," IEEE Aerospace Conference, Big Sky, MT, March 2017.
https://doi.org/10.1109/aero.2017.7943887

Polsgrove, T. P., Percy, T. K., Garcia, J. C., Cianciolo, A. D., Samareh, J. A., Lugo, R. A., Robertson, E. A., Cerimele, C. J., Sostaric, R. R., and Garcia, J. A. (2018) "Human Mars Entry, Descent and Landing Architecture Study: Rigid Decelerators," AIAA-2018-5192.
https://doi.org/10.2514/6.2016-5192

Price, H., Manning, R., Sklyanskiy, E., Braun, R. (2016) "A High-Heritage Blunt-Body Entry, Descent, and Landing Concept for Human Mars Exploration," AIAA-2016-0219.
https://doi.org/10.2514/6.2016-0219

Samareh, J. A. (2009) “A Multidisciplinary Tool for Systems Analysis of Planetary Entry, Descent, and Landing (SAPE),” NASA-TM-2009-215950.
http://hdl.handle.net/2060/20090041828

Samareh, J. A. and Komar, D. R. (2011) "Parametric Mass Modeling for Mars Entry, Descent and Landing System Analysis Study," AIAA 2011-1038.
https://doi.org/10.2514/6.2011-1038

Samareh, J. A., Glaab, L., Winski, R. G., Maddock, R. W., Emmett, A. L., Munk, M. M., Agrawal, P., Sepka, S., Aliaga, J., Zarchi, K., Mangini, M., Perino, S., Bayandor, J., and Liles, C. (2014) "Multi-Mission System Analysis for Planetary Entry (M-SAPE) Version 1," August 2014, NASA/TM–2014-218507.
http://hdl.handle.net/2060/20140010735

Sostaric, R. R., Johnson, B. J., Doll, J. A., Garcia, J. A., Nikaido, B. E., Brown, T. G., Harkins, T., and Decker, R. (2019) “Aeroballistic Range Testing of the CobraMRV Mid Lift-to-Drag Entry Vehicle,” AIAA-2019-0664.
https://doi.org/10.2514/6.2019-0664

Von Braun, Wernher. (1952) *The Mars Project* (2nd ed.). University of Illinois Press, 1952.
https://archive.org/details/TheMarsProject-WernherVonBraun1953

Wright, M. J. (2009) “Mars EDL/SA Thermal Protection System (TPS) Margin Management Plan”, Revision V2, June 2009.